Three- and four-point bending tests on artificial frozen soil samples at temperatures close to 0°C

Author 1

Yuko Yamamoto, Dr. [1)]

Institute for Geotechnical Engineering, ETH Zurich, Zurich, Switzerland

Email: yamamoto@drvollenweiderag.ch

Stefano Franscini Platz 5, 8093 Zurich, Switzerland

Author 2

Sarah, M. Springman, Prof. Dr. [2)]

Institute for Geotechnical Engineering, ETH Zurich, Zurich, Switzerland

Email: sarah.springman@igt.baug.ethz.ch

Stefano Franscini Platz 5, 8093 Zurich, Switzerland

Contact details of corresponding author:

Author 1: Yuko Yamamoto

Present affilication: Dr. Vollenweider AG, Badenerstrasse 621, 8048 Zürich

Tel. 0041 (0) 43 343 3030

E-mail: yamamoto@drvollenweiderag.ch

Abstract (135 words)

Degradation of alpine permafrost under global climate change has led to accelerated downslope creep, volume loss due to thawing and surface fissures in rock glaciers. This may lead to mass movements evolving through instabilities. It is hypothesised in this paper that the formation of cracks in the frozen body of a rock glacier can lead to triggering of such failures, and that analogue instrumented beam bending tests (with 3 and 4 supports/loading points) can be used to investigate fracture mechanics in frozen soil, with applications derivable for rock glaciers. Likely transitions between unpredictable brittle behaviour (through rapid crack formation, propagation or matrix destruction) and a more ductile response (dominated by micro-crack nucleation), can be established and quantified as a function of acoustic emission activity, deformation rate, solids-ice content and specimen temperature between -3.2°C and -0.5°C.

Highlights

- Tension cracking events in permafrost modelled by beam bending tests at < 0°C
- Fracture mechanics in frozen soil investigated through novel instrumentation
- Differentiating between sudden loss of strength and nucleation of micro cracks
- Transitions between ductile/brittle responses identified for volumetric ice content w_i, strain rates and temperature T

Keywords

Permafrost, Frozen soil, Bending tests, Acoustic emissions, Tension

List of notation

a	is the notched crack length of rectangular frozen soil sample [mm]
B	is the thickness of rectangular frozen soil sample [mm]
d_{max}	is the maximal grain size [mm]
L	is the length of the rectangular frozen soil sample [mm]
K_{Ic}	is the fracture toughness [kPa/m$^{0.5}$]
P	is the applied load [kN]

52 *PIV* is the Particle Image Velocimetry

53 R^2 is the coefficient of correlation

54 T is the temperature [°C]

55 w_i is the volumetric ice content [%]

56 W is the width of rectangular frozen soil sample [mm]

57 σ_f is the flexural stress [kPa]

58 σ_{YS} is the 0.2% offset yield strength in tension [kPa]

59

1. Introduction

Rock glaciers (Fig. 1a) are special geomorphic landforms in alpine periglacial environments and characterised by time-dependent, gravity-induced downslope deformation (Barsch, 1992). Typically, deformation occurs within an inhomogeneous ice-soil matrix (Fig. 1b) through secondary creep, while exhibiting temperature-dependent strain rate and ductile behaviour in enhanced shear zones within the rock glacier's core (e.g. Wagner, 1992; Arenson et al., 2002). However, complex thermal conditions, especially due to gradual warming in thermal degradation zones (Fig. 1c), may lead to significant changes in mechanical behaviour (Arenson, 2002; Vonder Mühll, 2003; Arenson et al., 2010; Haeberli et al., 2010; Springman et al., 2011; Springman et al., 2012; Buchli et al., 2013). Deformation of some rock glaciers has accelerated over past decades to several m/year and depressions and fissures are forming on the surface (Delaloye et al., 2008; Roer et al., 2008; Buchli et al., 2013), which are both parallel and perpendicular to the downslope movement (Kääb et al., 1998; Burger et al., 1999). Potentially, this accelerated, ongoing degradation could be aided by rapid fracture in the permafrost, such as was observed on the Graben Gufer rock glacier in 2009/2010, when surface movements reached 100 m/year (Delaloye et al., 2010).

Fracture is a significant process when dealing with fine-grained or frozen soils, since rapid crack formation and propagation may damage the soil matrix. This may cause sudden loss of strength (Thusyanthan et al., 2007; Azmatch et al., 2011). Transitions between unpredictable brittle behaviour (through rapid crack formation, propagation or matrix destruction) and a more ductile response (dominated by micro-crack nucleation), are dependent, primarily, on solid-ice-unfrozen water content, strain rate and temperature (e.g. Schulson & Duval, 2009; Akagawa & Nishisato, 2009). Furthermore, fissures provide a macro-flow-path for water, leading to progressive erosion in fine-grained soils (Harison et al., 1994). Infiltration of precipitation or snowmelt through fissures can affect the hydrological processes in rock glaciers (Buchli et al., 2013; Zhou et al., 2015), causing saturation and rapid increase of pore-water pressure in previously unsaturated soil. This could trigger slope instability (e.g. Fig. 1c).

89 It is hypothesised that crack formation in the frozen body of a rock glacier can lead to changes
90 in behaviour and potential for initiation of landslides and debris flows. Fracture mechanics, and
91 particularly transitions in brittle-ductile response in artificially frozen soil samples analogous to
92 permafrost between -3.2°C to -0.5°C, has been investigated and quantified through beam
93 bending tests (with 3 and 4 supports/loading points). The frozen soil specimens were
94 instrumented to detect acoustic emissions to capture the progress of crack propagation during
95 the tests.
96
97 **2. Tensile and fracture toughness of frozen soil**
98 The components of frozen soil strongly affect its response to thermo-hydro-mechanical loading,
99 particularly in terms of the relationships between solids-ice-air-unfrozen water content and the
100 free energy of soil water, suctions and pore pressures (Williams, 1964a; 1964b; 1966; Dash et
101 al., 1995). Significantly less experimental research has been conducted on tensile extension
102 tests in comparison with many research projects carried out to quantify compressive strength
103 (e.g. Fish, 1985; Andersland and Ladanyi, 1994; Andersen et al., 1995; Arenson and
104 Springman, 2005).
105
106 Tensile strength test methods can be divided into direct (tension test, many specimen forms)
107 and indirect methods (split cylinder, four-point bending, Brazilian tests) (Azmatch et al., 2010).
108 Three main variables affect the response: deformation rate, temperature and unfrozen water
109 content.
110
111 Prior research (Table 1) was mainly conducted on poorly graded silts, which exhibit a steep
112 decrease in tensile strength at temperatures close to 0°C (Haynes, 1978). Unlike the well-
113 graded soils studied here (Fig. 2), tensile strength is mobilised in silts at close to 0°C due to
114 suctions developing in the ice-soil-unfrozen water – air void matrix (Haynes, 1978; Akagawa &
115 Nishisato, 2009; Christ & Kim, 2009; Azmatch et al., 2010, 2011). An increase of unfrozen water
116 content as temperatures approach 0°C results in a loss in suction and an associated decrease
117 of tensile strength.
118

Akagawa & Nishisato (2009) investigated the tensile strength of a frozen fringe in Dotan silt within a relatively warm temperature range -0.15°C>T>-1.31°C. Frozen Dotan silt is 20-70 times stronger in tension than in its unfrozen state (164 kPa, T=-1.31°C; T=+0.6°C, 7.2 kPa). Azmatch et al. (2010) reported a ratio of 118 for Devon silt (827 kPa, T=-0.65°C; 7 kPa, T=2.25°C).

Yuanlin & Carbee (1987) conducted uniaxial direct tension tests on saturated Fairbanks silts at temperatures between -1°C>T>-10°C and report that strain rate affected the failure mode more than temperature. The stress-strain behaviour for frozen soils is similar to that of ice (Arenson et al., 2007), showing ductile behaviour when experiencing lower-rate deformations, and brittle behaviour when experiencing higher-rate deformations (Schulson et al., 1984). Akagawa & Nishisato (2009) reported that the fracture mode changes from ductile to brittle with decreasing temperature, even within a narrow temperature range. Haynes et al. (1975) observed a ductile-brittle transition for frozen Fairbanks silt (T=-9.4ºC) at a strain rate of 10^{-2}/s, similar to data obtained by Yuanlin & Carbee (1987).

Yuanlin & Carbee (1985) showed that the peak tensile strength decreased with decreasing strain rate for ductile failure modes, while it slightly decreased with increasing strain rate for the brittle failure mode. Bragg & Andersland (1980) found that tensile failure may not occur when the strain rate is too low, and that tensile strength was nearly independent from strain rate, although this was more typical at temperatures lower than -6°C (Haynes, 1978).

Fracture toughness is typically determined to quantify the resistance to crack propagation, assuming linear elastic plane strain conditions (Anderson, 1995). However, fracture toughness of frozen soil has not been well investigated until now, in contrast to ice (Schulson & Duval, 2009). Li & Yang (2000) and Konrad & Cummings (2001) showed that fracture toughness of frozen soils increases with higher volumetric ice contents and lower temperatures. Konrad & Cummings (2001) also reported that the fracture toughness decreased with decreasing average grain size.

147 It is clear that volumetric ice content, temperature and strain rate all play a role in the location of
148 the transition between brittle and ductile behaviour. This has been investigated through three
149 and four-point bending tests and the results will be reported and discussed in this paper.
150
151 **3. Samples and testing procedure**
152 ***3.1 Artificial frozen soil samples***
153 Rectangular specimens, with and without notches, were prepared from frozen soil for the three-
154 and four-point bending tests, respectively. Yamamoto & Springman (2014) describe the
155 methodology for mixing the components to planned relative ice-solid volume fractions. Crushed
156 ice with d_{max}=2 mm and silty gravel sampled from the Murtèl-Corvatsch rock glacier, Swiss Alps,
157 with a Fuller-curve grain size distribution (Fuller & Thompson, 1906) scaled to d_{max}=4 mm (Fig.
158 2) were mixed and placed in an insulated rectangular mould. The mixture was saturated slowly
159 from below with de-aired water at ~0 °C.
160
161 A metal plate (35 mm depth, 2 mm width) was placed at the longitudinal midspan of the mould
162 to prepare notched specimens for three-point bending tests, which were then frozen one-
163 dimensionally from top to bottom, at T=-18°C, allowing any excess water to drain through the
164 bottom. The specimens were trimmed with a circular diamond saw to measure 70×70×240 mm.
165
166 ***3.2 Three-point bending tests: procedure and overview***
167 The apparatus (Fig. 3a) containing the frozen rectangular beam specimen was mounted on two
168 bottom loading points, and placed in a cold room at test temperature. This was controlled by
169 almost shutting the cell and circulating coolant through copper tubes (Fig. 3a) for 24 hours, first
170 to stabilise, and then to keep the air temperature constant.
171
172 An acoustic sensor was attached directly onto the beam (Fig. 3b). Surface temperatures were
173 measured at two positions (Fig. 3c). The top loading point was fixed at the midspan, and was
174 placed onto the specimen carefully, with an initial axial load of 10N.
175

Three-point bending tests according to ASTM C78-09 (2009) were carried out within a temperature range -3.2°C<T<-0.5°C. The load was applied at constant vertical deformation rates of 1.0 and 0.1 mm/min (postulated as brittle and ductile dominant behaviour, respectively) until the vertical deformation exceeded 4 mm. The effect of volumetric ice content (w_i: 36–83%) on the fracture toughness KIc was investigated.

The specimens were thawed after the pre-notched crack had grown under mode-I (crack-opening) for subsequent back-calculation of the volumetric compositions of ice, solids and air. These were reported in Table 2, together with the test conditions. Three test groups were formed, depending on deformation rate and volumetric ice content .

3.3 Four-point bending tests: procedure and overview

The resistance to crack initiation and tensile strength of frozen soil was determined using a four-point bending apparatus (ASTM C78-09, 2009) (Fig. 3e,f). The bending moment applied between two loading points was constant spatially. The flexural stress σ_y was calculated from the load applied to the specimen.

The evolution of the bending strain at the midpoint of the beam specimen was derived from Particle Image Velocimetry (PIV), after similar four-point bending tests on clay beams conducted by Thusyanthan et al. (2007). Soil displacements can be determined precisely by operating on the visual image texture of the soil through analysis of a series of digital images (White et al., 2003). Acrylic glass, with 12 target markers attached, was fixed in front of the beam specimen to provide a reference coordinate system for the deformation calculations (Fig. 4a).

The apparatus cell was kept open during tests in which PIV was used. Test temperature was reported as an average value, with variations reaching up to ± 0.3°C. Digital images of the beam middle were taken every 10s for a test with a deformation rate of 0.1 mm/min. 22 pairs of 56×56 pixel measurement patches were defined in the digital image on either side of the mid-span of the beam throughout the full height (Fig. 4a). The longitudinal strain in the beam was

205 determined by dividing the original distance z_0=30 mm by the horizontal movement of two
206 patches z_1 and z_2 (Fig. 4b, Thusyanthan et al., 2007).

207 $$\varepsilon_l = \frac{z_1 + z_2}{z_0} \quad (1)$$

208 Four-point bending tests (Table 3) were carried out within a temperature range of -3.1°C<T<-
209 0.6°C. Tests are divided into three groups, depending on the deformation rate (1.0 and 0.1
210 mm/min) and volumetric ice content (w_i: 41–82%).
211
212 **4. Test results**
213 ***4.1 Three-point bending tests***
214 Force-displacement curves from test series 1 (1 mm/min, w_i=~80%, Fig. 5a) show a sudden
215 loss of force after reaching the peak, indicating rapid crack propagation. In series 2 (0.1
216 mm/min, w_i=~80%), only Test B16, carried out at the warmest temperature (T=-0.63°C)
217 exhibited ductile behaviour with a rounded, rather than a sharp peak in force-displacement
218 space, despite two clear rupture events before the peak (Fig. 5b). Test B5 (T=-2.65°C) showed
219 a more significant loss of force, followed by an increase after the first major rupture, which
220 implies that crack propagation stopped and further crack opening was resisted until the second
221 peak was observed. The other tests (B4,B7,B12) in series 2 exhibited similar behaviour to test
222 B5.
223
224 Denser specimens were tested in series 3 (0.1 mm/min, w_i=36-58%, Table 2). Rounded peaks
225 and gradual decrease in force are apparent in the force-displacement curves (Fig. 5c) for tests
226 B14 (T=-0.53°C), B15 (T=-0.59°C, 1 mm/min) and B17 (T=-1.56°C), indicating ductile rather
227 than brittle responses, although occasional small events occurred that were accompanied by a
228 loss of force of:
229 • 0.01 kN at displacement 2.3 mm (test B14),
230 • 0.03 kN, post-peak, with recovery of up to 0.01 kN, twice (test B17, arrows in Fig. 5c).
231
232 A similar response to B17 was observed in tests B9 and B11.
233

234 ***4.1.1 Crack propagation***

235 Acoustic emissions were recorded for all specimens from series 1 to 3. A typical response for
236 series 1 is shown for test B3 (Fig. 6a). The sudden loss of force observed at a displacement of
237 0.22 mm results in the first significant peak of acoustic emission rate (25 bursts/s), indicating
238 rapid crack propagation. Acoustic emissions occurred infrequently rather than continuously after
239 the sudden loss of force. Small force jumps (or fluctuations) from displacement 0.25 mm to 3.5
240 mm can be correlated with acoustic emissions (blue arrows for two examples; Fig. 6a). Rapid
241 and relatively large crack propagations occurred as displacement proceeded, since the
242 amplitude of the acoustic emission rate is more or less similar to the first peak at a displacement
243 of 0.22 mm.

244

245 Brittle-ductile transitional behaviour is observed in the force-displacement diagrams for test B16
246 of series 2 (Fig. 6b). The first peak in the acoustic emission rates at a displacement of 0.37 mm
247 indicates that a crack was propagated rapidly, with a loss of force by 0.20 kN to 0.17 kN (blue
248 arrow; Fig. 6b). The second highest emission rate (4/s) occurred very shortly after the first peak
249 (dropping from 0.190 to 0.185 kN). Subsequently, the cumulative acoustic emissions increase
250 gradually, i.e. reducing frequency of emissions to 1–2/s. until the third and greater peak was
251 reached at a displacement of 0.73 mm. This implies that the cracks propagated sequentially at
252 an average rate of 0.1/s over the first 30 minutes of the test.

253

254 The acoustic emission response obtained for test B9 (Fig. 6c) from series 3 was similar to that
255 of test B16. No sudden loss of force was observed in these denser specimens, with the
256 exception of a small event at a displacement of 0.4 mm, which was accompanied by the peak
257 acoustic emission rate (7/s). Half of the acoustic emissions were recorded prior to the peak
258 force (0.43 kN). Subsequently, the cumulative acoustic emissions increased gradually, with a
259 more or less constant rate throughout test B9.

260

261 The shapes of the cracks that propagated from the notch (Fig. 7a), are shown in Figs. 7b,c,d for
262 the tests B3 (series 1), B16 (series 2) and B9 (series 3) respectively. Wing cracks that occur in

263 ice (Schulson, 1990; 2001) can be identified in tests B3 and B6. The largest visible crack of the
264 three is seen in test B3.
265
266 The cracks in tests B16 and B9 were of similar size, starting from the top of the pre-notched
267 crack, although propagation was limited and gradual opening of the existing crack was the main
268 mechanical response. Parallel crack formations could be identified in test B9 (circled in Fig. 7d).
269 These cracks were neither connected to each other, nor to the pre-notched crack, although it
270 can be assumed that a sequence of such events might occur ahead of the main crack as it
271 progressed upwards from the notch.
272
273 Fig. 8 shows temperature dependence of the response of the specimens, in terms of cumulative
274 acoustic emissions up to a deformation of 4 mm. An increase in cumulative acoustic emissions
275 with temperature increase was obvious for series 1 and 2, whereas the cumulative acoustic
276 emissions decreased with temperature increase for series 3.
277
278 ***4.1.2 Fracture toughness***
279 A formulation proposed by Go et al. (1984), which takes into account the influence of the L/W
280 ratio on the stress-intensity of mode I, i.e. fracture toughness, was used to determine the
281 fracture toughness (Table 4) of the specimens tested in series 1-3, after Dempsey et al. (1989):

$$K_{IC} = \frac{3P}{4BW^{0.5}} f\left(\frac{a}{W}\right) \qquad \textbf{2}$$

282 where P is the applied load and:

$$f\left(\frac{a}{W}\right) = -1.186\left(1-\frac{a}{W}\right)^{2} + 2.474\left(1-\frac{a}{W}\right) - 6.858 + 8.124\left(1-\frac{a}{W}\right)^{-1} + 0.045\left(1-\frac{a}{W}\right)^{-2} \qquad \textbf{3}$$

283
284 ASTM E399-09 (1985) recommends that a validity check is performed to determine whether the
285 specimen dimensions were appropriate. The size requirements for a valid K_{IC} test are defined
286 as follows:

$$B,\ (\mathrm{W}-a) \geq 2.5\left(\frac{K_{Ic}}{\sigma_{YS}}\right)^2 \qquad \textbf{4}$$

where σ_{YS} is the 0.2% offset yield strength in tension. Equation 4 was satisfied for all tests conducted when σ_{YS}>50 kPa. This confirms that the dimensions of these frozen soil specimens were acceptable for four-point bending tests.

The influence of temperature on the fracture toughness is shown together with best-fit linear regression lines and coefficients of correlation R^2 for each series (Fig. 9). The correlation between reducing fracture toughness with increasing temperature is clear. This is consistent with results from Konrad & Cummings (2001), who determined the fracture toughness for frozen sand and frozen crushed stone. The slope of the trend line for series 3 (-34.35 kPa·m$^{0.5}$/ºC) is much steeper than those for series 1 and 2 (-8.87 and -10.18 kPa·m$^{0.5}$/ºC), respectively (Fig. 9).

4.2 Four-point bending tests

The flexural stress σ_f is calculated as:

$$\sigma_f = \frac{PL}{BW^2} \qquad \textbf{5}$$

where P is the applied load, W is the width, B is the thickness of the specimen and L is the length of the support span. The maximum flexural stress, when $P=P_{max}$, is summarised in Table 4. Pre-test specimens are shown in Figs. 10a and 11a.

Brittle failure was observed in the specimens from series 1 (1 mm/min, w_i~80%, Table 4) as well as for test 4PT3 that was carried out at the coldest temperature (-3.1°C) in series 2 (0.1 mm/min, w_i~80%, Table 4). Sudden crack initiation and rapid propagation split the frozen soil specimen in two (e.g. Fig. 10b). In contrast, the specimens were bent as vertical displacement proceeded in the remaining specimens for series 2, and for all tests in series 3 (e.g. Fig. 11b). Several cracks were also detected close to the lower edge of the specimen in these cases, however, they were not connected to each other.

312 Longitudinal strain–flexural stress curves are summarised in Fig. 12. Strain measurement using
313 the PIV method was not successful in tests 4PT2, 4PT3 and 4PT11, therefore only one strain-
314 stress curve (4PT5) was available to represent the brittle behaviour (Fig. 12a). A bi-linear
315 increase of flexural stress up to failure can be observed. The first line from the origin may be
316 representing uneven loading conditions whereas the second line is probably representing actual
317 stress-strain relationship. The threshold at strain=0.02%, between two linear portions of the
318 flexural stress-longitudinal strain plot, coincided with an exponential increase in acoustic
319 emission until failure was reached. Crack initiation occurred at this strain and was propagated
320 over the subsequent 45s until the end of the test.
321
322 Longitudinal strain–flexural stress curves for series 2 indicate ductile behaviour of the
323 specimens (Fig. 12b). More or less similar maximum flexural stress was reached for tests 4PT4
324 (T=-1.08°C) and 4PT1 (T=-0.61°C), whereas the stiffness gradient was steeper for 4PT4 than
325 for 4PT1. Test 4PT7 (T=-0.58°C) sustained less flexural stress, but the slope of the initial
326 stiffness gradient was as steep as for test 4PT4. It was expected that the specimens would
327 exhibit stiffer behaviour when the temperature was lower, however, this was not the case. A
328 similar trend can be seen for series 3, where the specimen in test 4PT6 (T=-1.33°C) was stiffer
329 than test 4PT9 (T=-2.98°C) during the early phases (Fig. 12c).
330
331 Test 4PT9 was ductile up to a longitudinal strain of just over 1.5%, whereupon the behaviour
332 became brittle. A sharp decrease of flexural stress can be seen between strains of 1.65–1.76%,
333 which was accompanied by a rapid increase of cumulative acoustic emissions (red solid lines,
334 Fig. 12c). The deformation rate was 0.1 mm/min, however the temperature (T=-2.98°C) was low
335 enough for the specimen to exhibit brittle behaviour at larger strain rates, i.e. a sudden loss in
336 flexural stress, notwithstanding a solid content of 48%.
337
338 The number of cumulative acoustic emissions captured in series 2 was greater than in series 3,
339 except for test 4PT9 (series 3; T=-2.98°C). The specimens from tests 4PT7 (series 2; T=-
340 0.58°C) and 4PT10 (series 3; T=-0.65°C) exhibited different stress-strain behaviour to the other
341 tests. A hardening phase up to a strain of 1% was followed by a plateau up to a strain of 4.5%.

342 The cumulative acoustic emissions were lower than for the tests in each series, with more
343 acoustic emissions by almost an order of magnitude in the ice-rich specimen (4PT7) compared
344 to 4PT10 at a similar temperature.
345
346 ***4.2.1 Flexural strength***
347 Temperature dependence of maximum flexural stress is presented for all series (Fig. 13). Best-
348 fit linear regression lines have been drawn and reported with coefficients of correlation R^2. As
349 shown by Akagawa & Nishisato (2009) and Azmatch et al. (2011), a temperature increase has
350 led to a decrease in maximum flexural stress. The regression lines for maximum flexural
351 strength, determined for specimens from series 1 and 2, were very similar for temperatures
352 ranging from -1.5°C–-0.5°C. This can be distinguished by the almost identical trendlines
353 obtained for these two series (Fig. 13), even though specimens from series 1 exhibited
354 completely brittle behaviour, whereas those from series 2 were ductile, as described earlier. A
355 similar trend is recognised in Fig. 13, as for temperature dependence of fracture toughness, in
356 that the slope of the trend line is much steeper for series 3 than for series 1 and 2.
357
358 **5. Discussion**
359 ***5.1 Brittle and brittle-ductile response of ice-rich specimens***
360 Stiff force-displacement relationships, prior to almost complete loss of strength, characterised
361 brittle behaviour for ice-rich specimens ($68\% < w_i < 80\%$) that were loaded at the faster rate of
362 displacement (series 1; 1 mm/min; Fig. 5a) for three-point bending tests (-0.8 to -3.2°C).
363 Similarly stiff pre-peak responses, yet only partial loss of strength, occurred for the ice-rich
364 specimens loaded at a slower displacement rate of 0.1 mm/min (series 2; Fig. 5b), although the
365 large strain behaviour was ductile. This could be characterised as a brittle-ductile response,
366 which transitioned to dominant ductile behaviour for temperatures warmer than -0.8°C.
367
368 This categorisation of brittle-ductile behaviour was generally supported by the data from
369 acoustic emissions that showed infrequent acoustic events at higher emission rates (Fig. 6a)
370 during brittle behaviour (series 1: three-point: initial burst 25/s coincident with 95% loss of force,
371 peak rate 40/s) as a large wing crack propagated rapidly (Fig. 7b). Interestingly, the cumulative

372 emissions only amounted to less than 60 at the end of the test (Fig. 6a), with a stepwise
373 increase throughout the test. The brittle response in the four-point bending tests, however, led
374 to over 900 acoustic events at <0.1% strain (Fig. 12a) and the rate increased throughout the
375 test until the crack propagated rapidly to the top of the specimen.
376
377 Since the specimen for the four-point bending test does not have a notched crack, the acoustic
378 events are due to both initiation and propagation, whereas propagation is the main source in the
379 three-point bending test specimens. This comparison confirms the statement by Hallam (1986)
380 that very brittle failure is observed when failure is dominated by crack propagation, whereas
381 some ductility and many cracks are observed when failure is dominated by the nucleation of
382 cracks.
383
384 Slower emission rates (e.g. maximum 13/s pre-peak force for test B16, Fig. 6b) and more
385 frequent single events at a rate of 1/s post-peak force characterise the brittle-ductile response,
386 with crack opening occurring above the notch in the three-point bending tests (Fig. 7c). Net
387 cumulative emissions increased during three-point bending tests on ice-rich specimens in
388 Series 1 and 2 when tested at warmer temperatures (Fig. 8). This can be explained by brittle
389 behaviour, which is likely to occur at lower temperatures, since the crack extended very
390 suddenly, and only a few acoustic emissions were detected after the sudden loss of force. In
391 contrast, smaller crack propagations were probably more active after the loss of peak force at
392 warmer temperatures, resulting in higher cumulative acoustic emissions.
393
394 ***5.2 Ductile response of frozen soil specimens***
395 Reducing the ice content (36%<w_i<58%), i.e. the soil particles were more likely to be in contact
396 with each other, led to ductile response at all temperatures (-0.5 to -3.0°C) in both three- and
397 four-point bending tests (Series 3; Figs. 5c, 7d, 11b, 12c). This could explain the gradual
398 increase of cumulative acoustic emissions (Fig. 6c) during ductile yielding, with a reducing rate
399 throughout the test, which might be related to the propagation of small cracks ahead of the main
400 one. The densely packed soil grains could partially prevent the cracks from further propagation;

401 this would be unlikely to occur for ice-rich specimens with much higher volumetric ice contents
402 (e.g. Test 4PT9).
403
404 Comparing the behaviour for specimens with w_i~40%, test B15 (1.0 mm/min; -0.6°C) was
405 similar to test B17 (0.1 mm/min; -1.56°C), even though the deformation rate was higher.
406 Notwithstanding, the contribution of 58% solids and a warmer temperature caused the dominant
407 response for B15 to become ductile, with periods of crack opening and temporary recovery,
408 rather than brittle behaviour with sudden releases of energy. Rapid crack propagation was
409 proposed to occur in test B17 until strain energy available at the crack tip was insufficient to
410 overcome resistance, before the load decreased gradually as displacement proceeded with
411 ongoing, smaller fluctuations due to a sequence of crack propagation and resistance.
412
413 The decrease in cumulative acoustic emissions that was observed in series 3 of three-point
414 bending test with increasing temperatures might be due to the lower volumetric ice content of
415 these specimens, compared to series 1 and 2. Ductile behaviour was dominant in series 3,
416 since crack propagation was probably constrained by the dense packing of the soil grains, and
417 was prevalent only in the colder specimens.
418
419 ***5.3 Fracture toughness***
420 The fracture toughness of specimens with less volumetric ice content is more affected by the
421 temperature than for those with higher volumetric ice content, although higher fracture
422 toughness was obtained for specimens from series 3 (w_i=36–57%) than series 1 and 2 (w_i=68–
423 83%) at equivalent temperatures colder than -1.25ºC (Fig. 9). This finding contradicts the
424 statement made by Konrad & Cummings (2001) that fracture toughness increases with
425 increasing volumetric ice content. However, these authors conducted their tests on specimens
426 at T=-2°C and -5°C, with much lower volumetric ice contents (w_i=6–28%) than those used in
427 these series.
428
429 The fracture toughness of polycrystalline ice at T>-3°C obtained by Liu & Miller (1979) and
430 Urabe et al. (1980) lay between 80–105 kPa·$m^{0.5}$, which is slightly lower than values obtained

for the frozen soil specimens with 68%<w_i<83% in series 1 and 2 (Fig. 9). It can be concluded that fracture toughness increases as volumetric ice content decreases until a certain value, since the soil grains restrict crack propagation when specimens respond with more ductility in the three-point bending tests. However, further decrease of volumetric ice content results in a depleted cohesive component (ice), and lower fracture toughness, which reflects the mobilisation of reduced tensile resistance (Fig. 13) and fracture toughness (Fig. 9) with increasing temperature in frozen soils.

5.3 Flexural strength

The maximum flexural stress is more or less replicated for series 1 and 2 as it reduces with increasing temperature (Fig. 13). The denser specimens that respond in a ductile fashion (series 3) mobilised higher maximum flexural stress at the colder temperatures and lower for the warmer specimens. This might be because the unfrozen water content increases more rapidly in the specimens with lower volumetric ice contents as the suction in the frozen water reduces and temperature increases, than in the specimens with greater volumetric ice content, where soil grains are seldom in contact with each other. The increased amount of unfrozen water may cause less stiff behaviour, due to the loss of suction (Williams, 1964b).

5.4 Crack formation and propagation in a rock glacier

Tensile strength of fine unfrozen soil is low (e.g. Hallett & Newson, 2001; Azmatch et al., 2011) compared to that of frozen soil. The depression zone, existing at shallow depths in a warm rock glacier, might deepen as extensive flow in the permafrost layer continues faster in the extension zone than the neighbouring translation zone, downslope. The deepening depressions in an upper zone of a rock glacier results in the decrease in distance between the active layer and the shear zone, even though the surface of the depression zone seems always to be covered by the active layer containing coarse soil (Buchli et al., 2013). This indicates that the temperature in the shear zone, thus the creep deformation rate, is more susceptible to the surface temperature, since the thickness of the permafrost, which plays a role as a damping material, decreases.

The tensile strength of the frozen soil, investigated using the four-point bending tests over a temperature range between -3 and -0.5°C, indicates that a tension crack in the frozen soil layer in a rock glacier is unlikely to occur within the temperature range, since the stresses acting on the frozen soil are generally lower than the tensile strength. However, frozen soil with low volumetric ice content is more susceptible to initiation of a tension crack than that with a higher volumetric ice content, as temperature increases to the thawing point. This implies that frozen soil in a rock glacier may be exposed to a deepening depression in a highly heterogeneous zone, containing low volumetric ice contents, and results in an initiation of tension crack at the surface of the frozen soil layer.

The tracer tests reported by Buchli et al. (2013) for the Furggwanghorn rock glacier indicated that the major water "drainage" flows downslope on top of the frozen soil and possibly at smaller velocity through the thawed fine-grained unsaturated soil at greater depths below the permafrost. The occurrence of cracks in the active layer and permafrost plays a role as a macro-flow path for water, in addition to the air voids existing in the permafrost body in a rock glacier. The infiltration of precipitation through the cracked surface may cause rapid increase of pore water pressure in the unsaturated soil in the active layer, which results in an increase of saturation degree and a decrease of effective stress. In addition, new water migration paths contribute to changing the thermal regime, since heat flux is transferred by advection. This might result in a progressive increase in frozen soil temperature in a localised area due to the warmer temperature of the infiltrated precipitation, which is reported as a talik formation by Zenklusen & Phillips (2012). Accordingly, it can be concluded that hydraulic effect on the strength of frozen soil becomes greater, if the permafrost layer is exposed to crack formation or deepening depressions. This may eventually lead to local instabilities in rock glaciers.

6. Conclusions

The resistance to the crack initiation of frozen soil specimens was investigated by four-point bending tests on rectangular frozen soil specimens within a temperature range of -3.1°C<T<-0.6°C. Both brittle and ductile crack formations were observed, depending on the temperature and vertical deformation rate applied. A sudden loss of strength indicated brittle behaviour in an

ice medium at lower temperatures, and under higher vertical deformation rates. Ductile failures were observed when the process was dominated by the nucleation of micro-cracks. The ductility was enhanced when the volumetric ice content was low. A decrease in maximum flexural stress was found as temperature increased towards 0°C. This temperature effect was more pronounced for the lower volumetric ice contents.

The resistance to the crack propagation of frozen soil specimens was investigated in three-point loading tests on pre-notched rectangular frozen soil specimens within a temperature range -3.2°C<T<-0.5°C. The progress of crack propagation could be captured by the acoustic emission response observed at the surface of the frozen soil specimens, together with the force-displacement relationships. Rapid crack propagation caused a large number of acoustic emissions within a short period of time and further development of micro-cracks was limited at colder temperatures and faster deformation rates. In contrast, the small crack propagations were more active at warmer temperatures and at slow deformation rates.

The specimens with $w_i \approx 79\%$ exhibited an increase in cumulative acoustic emissions with increasing temperatures. In contrast, a decrease in cumulative acoustic emissions with increasing temperatures was observed for the specimens with $w_i \approx 45\%$, since the occurrence of large scale crack propagation was probably constrained by the dense packing of soil grains, thus a ductile response was obtained. The propagation of cracks could be promoted in the specimens at lower temperatures, since the behaviour of the ice granules were less ductile than at higher temperatures.

The stress level observed for the resistance to the crack propagation indicated that catastrophic brittle failure is unlikely to occur in the creeping rock glacier within the temperature ranges measured, since the stresses acting on the frozen soil are generally lower than the tensile strength. However, the frozen soil with low volumetric ice content might be more susceptible to the initiation and propagation of tension crack than the zones with higher volumetric ice content, at temperatures close to the thawing point.

Acknowledgements

The financial support received from the Swiss National Science Foundation through grant number 200021_125078 is gratefully acknowledged. Ernst Bleiker, Adrian Zweidler and the workshop and laboratory staff from the Institute for Geotechnical Engineering, Swiss Federal Institute of Technology are thanked for their contributions to the design, construction, and electrical setup of the upgrades to the triaxial apparatus adapted for the beam tests.

References

Akagawa, S. & Nishisato, K. (2009). Tensile strength of frozen soil in the temperature range of the frozen fringe. *Cold Regions Science and Technology* **57**, 13-22.

Andersen, G.R., Swan, C.W., Ladd, C.C. & Germaine, J.T. (1995). Small-strain behavior of frozen sand in triaxial compression. *Canadian Geotechnical Journal* **32**, No. 3, 428-451.

Andersland, O.B. and Ladanyi, B. (1994*). An introduction to frozen ground engineering*. Chapman & Hall, New York.

Anderson, T.L. (1995). *Fracture mechanics*. CRC Press (Pub), Boca Raton.

Arenson, L.U. (2002). *Unstable alpine permafrost: a potentially important natural hazard - variations of geotechnical behaviour with time and temperature*. D.Sc. Dissertation No. 14801, Institute for Geotechnical Engineering, ETH Zurich, Switzerland.

Arenson, L.U., Hoelzle, M. & Springman, S.M. (2002). Borehole deformation measurements and internal structure of some rock glaciers in Switzerland. *Permafrost and Periglacial Processes*, **13**(2), 117-135.

Arenson, L.U. & Springman, S.M. 2005. Triaxial constant stress and constant strain rate tests on ice-rich permafrost samples. *Canadian Geotechnical Journal* **42**, No. 2, 412-430.

Arenson, L.U., Springman, S.M. & Sego, D.C. (2007). The rheology of frozen soils. *Applied Rheology* **17**, No. 1, 1-14, 12147.

Arenson, L.U., Hauck, C., Hilbich, C., Seward, L., Yamamoto, Y. & Springman, S.M. (2010). Sub-surface heterogeneities in the Murtèl-Corvatsch rock glacier, Switzerland. *Proceedings of the Sixth Canadian Permafrost Conference*, *Calgary, Canada,* 1494-1500.

ASTM. (1985). *E399-83 Standard test method for plane-strain fracture toughness of metallic materials* (pp. 547-582).

ASTM. (2009). *C78-09 Standard method for flexural strength of concrete (using simple beam with third-point loading)*.

Azmatch, T.F., Sego, D.C., Arenson, L.U. & Biggar, K.W. (2010). Tensile strength of frozen soils using four-point bending test. *Proceedings of the Sixth Canadian Permafrost Conference, Calgary, Canada*, 436-442.

Azmatch, T.F., Sego, D.C., Arenson, L.U. & Biggar, K.W. (2011). Tensile strength and stress-strain behaviour of Devon silt under frozen fringe conditions. *Cold Regions Science and Technology* **68**, 85-90.

Barsch, D. (1992). Permafrost creep and rockglaciers. *Permafrost and Periglacial Processes* **3**, 175-188.

Bragg, R.A. & Andersland, O.B. (1980). Strain rate, temperature, and sample size effects on compression and tensile properties of frozen sand. *Proceedings of the Second International Symposium on Ground Freezing, Trondheim, Norway*, 34-47.

Buchli, T., Merz, K., Zhou, X., Kinzelbach, W. & Springman, S.M. (2013). Characterization and Monitoring of the Furggwanghorn Rock Glacier, Turtmann Valley, Switzerland: Results from 2010 to 2012. *Vadose Zone* **12**. No. 1, doi:10.2136/vzj2012.0067.

Burger, K.C., Degenhardt Jr., J.J. & Giardino, J.R. (1999). Engineering geomorphology of rock glaciers. *Geomorphology* **31**, 93-132.

Christ, M. & Kim, Y. (2009). Experimental study on the physical-mechanical properties of frozen silt. *KSCE Journal of Civil Engineering* **13**, No. 5 317-324.

Dash, J.G., Fu, H., & Wettlaufer, J.S. (1995). The premelting of ice and its environmental consequences. *Reports on Progress in Physics* **58**, 115-167.

Delaloye, R., Perruchoud, E., Avian, M., Kaufmann, V., Bodin, X., Hausmann, H., Ikeda, A., Kääb, A., Kellerer-Pirklbauer, A., Krainer, K., Lambiel, Ch., Mihajlovic, D., Staub, B., Roer, I. & Thibert, E. (2008). Recent Interannual Variations of Rock Glacier Creep in the European Alps. *Proceedings of the 9th International Conference on Permafrost, Fairbanks, Alaska, USA* 1, 343-348.

579 Delaloye, R., Lambiel, C. & Gärtner-Roer, I. (2010). Overview of rock glacier kinematics
580 research in the Swiss Alps: seasonal rhythm, interannual variations and trends over several
581 decades. *Geographica Helvetica* **65**, No. 2, 135-145.
582 Dempsey, J.P., Wei, Y., DeFranco, S., Ruben, R. & Frachetti, R. (1989). Fracture toughness of
583 S2 columnar freshwater ice: crack length and specimen size effects - Part 1. *Proceedings of*
584 *the Eighth International Conference on Offshore Mechanics and Arctic Engineering, Hague,*
585 *Netherlands* **4**, 83-89.
586 Fish, A.M. (1985). Creep strength, strain rate, temperature and unfrozen water relationship in
587 frozen soil. *Proceedings of the Fourth International Symposium on Ground Freezing,*
588 *Sappor,* 29-36.
589 Fuller, W.B. & Thompson, S.E. (1906). The laws of proportioning concrete. *Transactions of the*
590 *American Society of Civil Engineers* **LVII**, No. 2, 67-143.
591 Go, C.-G., Swartz, S.E. & Hu, K.-K. (1984). Stress intensity factors for single-edge-notch beam.
592 *Journal of Engineering Mechanics* **110**, 629-632.
593 Haeberli, W., Noetzli, J., Arenson, L., Delaloye, R., Gärtner-Roer, I., Gruber, S., Isaksen, K.,
594 Kneisel, C., Krautblatter, M. & Phillips, M. (2010). Mountain permafrost: development and
595 challenges of a young research field. *Journal of Glaciology* **56**, No. 200, 1043-1058.
596 Hallam, S.D. (1986). The role of fracture in limiting ice forces. International Association for
597 Hydraulic Research. *Eighth International Symposium on Ice, Iowa City* 2, 287-319.
598 Hallett, P.D. & Newson, T.A. (2001). A simple fracture mechanics approach for assessing
599 ductile crack growth in soil. *Soil Science Society of America Journal* **65**, No. 4, 1083-1088.
600 Harison, J.A., Hardin, B.O. & Mahboub, K. (1994). Fracture toughness of compacted cohesive
601 soils using ring test. *Journal of Geotechnical Engineering* **120**, No. 5, 872-891.
602 Haynes, F.D. (1978). Strength and deformation of frozen silt. *Proceedings of the Third*
603 *International Conference on Permafrost, Edmonton, Alberta, Canada* 1, 655-661.
604 Haynes, F.D. & Karalius, J.A. (1977). *Effect of temperature on the strength of frozen silt*.
605 CRREL Report 77-3, Cold Regions Research And Engineering Laboratory, Hanover, New
606 Hampshire.
607 Haynes, F.D., Karalius, J.A. & Kalafut, J. (1975). *Strain rate effect on the strength of frozen silt*
608 *(Technical Report No. 350)*, US Army Cold Regions Research and Engineering Laboratory.

609 Kääb, A., Gudmundsson, G.H. & Hoelzle, M. (1998). Surface deformation of creeping mountain
610 permafrost. Photogrammetric investigations on Murtèl rock glacier, Swiss Alps. *Proceedings*
611 *of the Seventh International Conference on Permafrost, Yellowknife, Canada*, 531-537.
612 Konrad, J.M. & Cummings, J. (2001). Fracture toughness of frozen base and subbase soils in
613 pavement. *Canadian Geotechnical Journal* **38**, 967-981.
614 Li, H. & Yang, H. (2000). Experimental investigation of fracture toughness of frozen soils.
615 *Journal of Cold Regions Engineering* **14**, No. 1, 43-49.
616 Liu, H.W. & Miller, K.J. (1979). Fracture toughness of fresh-water ice. *Journal of Glaciology*
617 **22(86)**, 135-143.
618 Roer, I., Haeberli, W., Avian, M., Kaufmann, V., Delaloye, R., Lambiel, C. & Kääb, A. (2008).
619 Observations and Considerations on Destabilizing Active Rock Glaciers in the European
620 Alps. *Proceedings of the Ninth International Conference on Permafrost, Fairbanks, Alaska,*
621 1505-1510.
622 Schulson, E.M. (1990). The brittle compression fracture of ice. *Acta Metallurgica et Materialia*
623 **38**, 1963-1976.
624 Schulson, E.M. (2001). Brittle failure of ice. *Engineering Fracture Mechanics* **68(17-18)**, 1839-
625 1887.
626 Schulson, E.M., Lim, P.N. & Lee, R.W. (1984). A brittle to ductile transition in ice under tension.
627 *Philosophical Magazine A* **49**, No. 3, 353-363.
628 Schulson, E.M. & Duval, P. (2009). *Creep and Fracture of Ice*. Cambridge University Press,
629 Cambridge.
630 Springman, S.M., Yamamoto, Y., Buchli, T., Hertrich, M., Maurer, H., Merz, K., Gärtner-Roer, I.
631 & Seward, L. (2011). Rock glacier degradation and instabilities in the European Alps: a
632 characterisation and monitoring experiment in the Turtmanntal, CH. *Proceedings of the*
633 *Second World Landslide Forum, Rome*, *Landslide Science and Practice* 4, 5-13.
634 Springman, S.M., Arenson, L.U., Yamamoto, Y., Maurer, H., Kos, A., Buchli, T. & Derungs, G.
635 (2012). Multidisciplinary investigations on three rock glaciers in the Swiss Alps: legacies and
636 future perspectives. *Geografiska Annaler: Series A, Physical Geography* **94**, No. 2, 215-243.
637 Thusyanthan, N.I., Take, W.A., Madabhushi, S.P.G. & Bolton, M.D. (2007). Crack initiation in
638 clay observed in beam bending. *Géotechnique* **57**, No. 7, 581-594.

639 Urabe, N., Iwasaki, T. & Yoshitake, A. (1980). Fracture toughness of sea ice. *Cold Regions*
640 *Science and Technology* **3**, 29-37.
641 Vonder Mühll, D. (2003). Thermal variations of mountain permafrost: an example of
642 measurements since 1987 in the Swiss Alps. In: *Global Change and Protected Areas Edited*
643 *by G. Visconti, M. Beniston, E. Iannorelli and D. Barba, Kluwer Academic Publishers, New*
644 *York,* 83-95.
645 Wagner , S. (1992). Creep of Alpine permafrost, investigated on the Murtèl rock glacier.
646 *Permafrost and Periglacial Processes* **3**, 157-162
647 White, D.J., Take, W.A. & Bolton, M.D. (2003). Soil deformation measurement using particle
648 image velocimetry (PIV) and photogrammetry. *Géotechnique* **53**, No. 7, 619-631.
649 Williams, P.J. (1964a). Specific heat and apparent specific heat of frozen soils. *Géotechnique*
650 **14**, No. 2, 133-142.
651 Williams, P.J. (1964b). Unfrozen water content of frozen soils and soil moisture suction.
652 *Géotechnique* **14**, No. 3, 213-246.
653 Williams, P.J. (1966). Pore pressures at a penetrating front line and their prediction.
654 Géotechnique **16**, No. 3, 187-208.
655 Yamamoto, Y. (2013). *Instabilities in alpine permafrost: strength and stiffness in a warming*
656 *regime.* D.Sc. Dissertation No. 21596, Institute for Geotechnical Engineering, ETH Zurich,
657 Switzerland.
658 Yamamoto, Y. & Springman, S.M. (2014). Axial compression stress path tests on artificial frozen
659 soilsamples in a triaxial device at temperatures just below 0 °C. *Canadian Geotechnical*
660 *Journal* **51**, No. 10, 1178-1195.
661 Yuanlin, Z. & Carbee, D.L. 1985. Strain rate effect on the tensile strength of frozen silt. In
662 Kinoshita, S. & Fukuda, M. (Editors), Fourth International Symposium on Ground Freezing,
663 Sapporo, Japan, A.A. Balkema, Rotterdam, 1: 153-157.
664 Yuanlin, Z. & Carbee, D.L. 1987. Tensile strength of frozen silt (Technical Report No. 87-15),
665 US Army Cold Regions Research and Engineering Laboratory.
666 Zenklusen, E. & Phillips, M. (2012). Thermal evidence of recent talik formation in Ritigraben
667 rock glacier. *Proceedings of the Tenth International Conference on Permafrost, Salekhard,*
668 *Russia* 1, 479-483.

669 Zhou, X., Buchli, T., Kinzelbach, W., Stauffer, F. & Springman, S.M. (2015). Analysis of
670 Thermal Behaviour in the Active Layer of Degrading Mountain Permafrost. *Permafrost and*
671 *Periglacial Processes* **26**, No. 1, 39-56.
672
673 **Talbe captions**
674 Table 1: Selected tensile strength tests conducted to date on frozen soils (modified after
675 Akagawa & Nishisato, 2009).
676 Table 2: Overview of physical properties of artificially frozen, rectangular, notched soil
677 specimens and test conditions for three-point bending tests.
678 Table 3: Overview of physical properties of artificially frozen, rectangular soil specimens, test
679 conditions for four-point bending tests and maximum flexural stress.
680 Table 4: Overview of the results of three-point bending tests on artificially frozen, rectangular,
681 notched soil specimens.
682

683

684 Table 1. Selected tensile strength tests conducted to date on frozen soils (modified after

685 Akagawa & Nishisato, 2009).

Author	**Year**	**Material**	**Test type**	**T (°C)**	**Strain or Deformation rate**	**Moisture content**
Haynes et al.	1975	Saturated Fairbanks silt	Uniaxial direct tensile	-9.4	1.7×10^{-4} to 3.4×10^{-1} /s	-
Haynes	1978	Saturated Fairbanks silt	Uniaxial direct tensile	-0.1 to -57.0	0.0423 cm/s 4.23 cm/s	Calculation method by Anderson & Tice (1972)
Bragg & Andersland	1980	Wedron silica sand	Split-cylinder	-6.0	1.3 to 6.5 mm/min	-
Yuanlin & Carbee	1985 1987	Saturated Fairbanks silt	Uniaxial direct tensile	-5.0 -1.0 to -10	5.9×10^{-5} to 5.9×10^{2} cm/min	-
Akagawa & Nishisato	2009	Diluvial Dotan silt	Direct tensile	+0.6 -0.15 to -1.31	2.31 mm/min	TDR
Christ & Kim	2009	Silt (MH)	Uniaxial direct tensile	-2, -5, -10, -15, -20	1.0 mm/min	TDR
Azmatch et al.	2010 2011	Devon silt	Four-point bending	+2.25 -0.65 to -9.0	0.8 to 8 mm/min	TDR

686

687

688 Table 2: Overview of physical properties of artificially frozen, rectangular, notched soil
689 specimens and test conditions for three-point bending tests.

Test series	**Test no.**	**Volume composition**			**Density**	**Deformation rate**	**T**
		Ice	**Solid**	**Air**			
		%	**%**	**%**	**Mg/m³**	**mm/min**	**°C**
1	B3	78.07	18.79	3.13	1.23	1.0	-3.20 ± 0.08
	B6*	82.05	13.46	4.50	1.12	1.0	-2.66 ± 0.04
	B8*	74.03	17.88	8.09	1.17	1.0	-1.70 ± 0.04
	B10	75.65	19.03	5.32	1.21	1.0	-2.59 ± 0.04
	B13	83.38	16.46	0.16	1.21	1.0	-0.97 ± 0.03
2	B4	68.19	20.24	11.57	1.18	0.1	-3.25 ± 0.25
	B5	78.17	16.62	5.22	1.17	0.1	-2.65 ± 0.16
	B7	81.60	12.55	5.85	1.10	0.1	-1.66 ± 0.06
	B12	80.60	18.97	0.43	1.26	0.1	-0.83 ± 0.08
	B16	78.73	16.99	4.29	1.18	0.1	-0.63 ± 0.07
3	B9	57.81	40.52	1.67	1.63	0.1	-2.89 ± 0.04
	B11	50.69	46.24	3.07	1.72	0.1	-1.72 ± 0.08
	B14	36.16	61.81	2.03	2.01	0.1	-0.53 ± 0.08
	B17	38.96	58.22	2.81	1.94	0.1	-1.56 ± 0.08
	B15	41.83	57.66	0.51	1.95	1.0	-0.59 ± 0.02

690 * Acoustic emission measurement was not successful due to the loss of contact between the acoustic emission sensor
691 and the surface of the specimen.
692

693

694 Table 3: Overview of physical properties of artificially frozen, rectangular soil specimens, test
695 conditions for four-point bending tests and maximum flexural stress.

Test series	**Test no.**	**Volume composition**			**Density**	**Deformation rate**	**T**	**Max. flexural stress**
		Ice	**Solid**	**Air**				
		%	**%**	**%**	**Mg/m^3**	**mm/min**	**°C**	**kPa**
1	4PT2	78.88	15.53	5.59	1.15	1.0	-2.92 ± 0.03	1721
	4PT5	80.07	16.09	3.84	1.17	1.0	-1.40 ± 0.04	1598
	4PT11	79.33	19.87	0.80	1.27	1.0	-0.84 ± 0.08	1424
2	4PT1	80.49	17.68	1.83	1.22	0.1	-0.61 ± 0.10	1546
	4PT3	81.61	17.86	0.53	1.23	0.1	-3.10 ± 0.15	1805
	4PT4	81.35	16.02	2.63	1.18	0.1	-1.08 ± 0.26	1548
	4PT7	77.04	18.69	4.27	1.21	0.1	-0.58 ± 0.10	1216
3	4PT6	41.40	58.10	0.50	1.96	0.1	-1.33 ± 0.18	1150
	4PT9	50.92	48.01	1.08	1.77	0.1	-2.98 ± 0.30	2007
	4PT10	46.18	51.41	2.42	1.82	0.1	-0.65 ± 0.04	724.2
	4PT8	81.86	15.40	2.73	1.17	0.5	-0.78 ± 0.04	1214

696

697

698

699 Table 4: Overview of the results of three-point bending tests on artificially frozen, rectangular,

700 notched soil specimens.

Test series	**Test no.**	**w_i**	**Deformation rate**	**T**	**Brittle (B) or Ductile (D)**	**K_{IC}**	**Max load**	**Acoustic emission rate at K_{IC}**	**Cumulative acoustic emission till 4mm**
		%	**mm/min**	**°C**		**kPa·m$^{0.5}$**	**kN**	**/s**	**-**
1	B3	78.07	1	-3.20	B	160.3	0.338	0	55
	B6	82.05		-2.66	B	162.3	0.347	n.m.	n.m.
	B8	74.03		-1.70	B	141.6	0.325	n.m.	n.m.
	B10	75.65		-2.59	B	128.4	0.295	12	158
	B13	83.38		-0.97	B	137.4	0.300	37	209
2	B4	68.19	0.1	-3.25	B-D	147.5	0.340	16	40
	B5	78.17		-2.65	B-D	115.3	0.271	16	28
	B7	81.60		-1.66	B-D	88.8	0.272	0	77
	B12	80.60		-0.83	B-D	99.2	0.230	13	224
	B16	78.73		-0.63	B-D	88.5	0.205	1	200
3	B9	57.81	0.1	-2.89	B-D, D	187.6	0.432	4	204
	B11	50.69		-1.72	D	147.1	0.334	1	63
	B14	36.16		-0.53	D	103.8	0.224	1	17
	B17	38.96		-1.56	D	169.1	0.397	1	29
	B15	41.83	1	-0.59	D	143.9	0.328	0	13

701 n.m.: no measurement.

702

703

704

705 **Figure captions**

706 Figure1: a) aerial view of the Furggwanghorn rock glacier, Turtmanntal, Valais, Switzerland,
707 (Photograph, Sarah Springman), b) Two-dimensional schematic of the structure of frozen
708 soils (after Ting et al., 1983), c) Schematic cross section through a degrading rock glacier
709 (after Springman et al., 2011).

710 Figure 2: Grain size distribution of three soil samples taken from the Murtèl-Corvatsch rock
711 glacier (max. grain size 16 mm) and Fuller-curve for the maximum grain size of 4 mm and
712 16 mm, with γs=2.71–2.72 g/cm3 (Yamamoto & Springman, 2014).

713 Figure 3: Three-point bending test setup; (a) schematic view (drawing: H. Buschor); (b) acoustic
714 sensor holder (drawing: H. Buschor); (c) elevation (d) cross section; and Four-point
715 bending test setup; (e) elevation; (f) cross section.

716 Figure 4: Target markers on an acrylic glass in front of the artificially frozen beam specimen
717 (black dots on white squares) and distributed measurement patches (blue squares). The
718 frozen specimen shows natural texture exposed by the diamond saw cut; (b) Strain
719 calculation for a four-point bending tests, based on the two measurement patches at the
720 same height (after Thusyanthan et al., 2007).

721 Figure 5: Load-displacement curves for three-point bending tests on artificially frozen,
722 rectangular, notched soil specimens; (a) test series 1; (b) test series 2; (c) test series 3
723 and test B15.

724 Figure 6: Acoustic emission response of three-point bending tests on artificially frozen,
725 rectangular, notched soil specimens; (a) test series 1: B3 (wi = 78.0%, T = -3.2°C,
726 deformation rate = 1 mm/min); (b) test series 2: B16 (wi = 78.7%, T = -0.63°C,
727 deformation rate = 0.1 mm/min); (c) test series 3: B9 (wi = 57.8%, T = -2.9°C, deformation
728 rate = 0.1 mm/min).

729 Figure 7: Three-point bending crack propagation tests on artificially frozen soil specimens; (a) a
730 notched crack before test; (b) B3 (wi = 78.0%, T = -3.2°C, deformation rate = 1 mm/min);
731 (c) test B16 (wi = 78.7%, T = -0.63°C, deformation rate = 0.1 mm/min); (d) test B9 (wi =
732 57.8%, T = -2.9°C, deformation rate = 0.1 mm/min).

733 Figure 8: Temperature dependence of cumulative acoustic emissions obtained from three-point
734 bending tests on artificially frozen, rectangular, notched soil specimen up to a vertical
735 mid-beam deformation of 4 mm.
736 Figure 9: Temperature dependence of fracture toughness for three-point bending tests on
737 artificially frozen, rectangular, notched soil specimens.
738 Figure 10: Brittle deformation of the artificially frozen soil specimen in four-point bending test no.
739 4PT3 (series 2).
740 Figure 11: Ductile deformation of the artificially frozen soil specimen in four-point bending test
741 no. 4PT6 (series 3).
742 Figure 12: Flexural stress-longitudinal strain plots (upper figures) and cumulative acoustic
743 emission (lower figures) for four-point bending tests on artificially frozen, rectangular soil
744 specimens; (a) series 1; (b) series 2; (c) series 3.
745 Figure 13: Temperature dependence of maximum flexural stress for four-point bending tests on
746 artificially frozen, rectangular soil specimens.

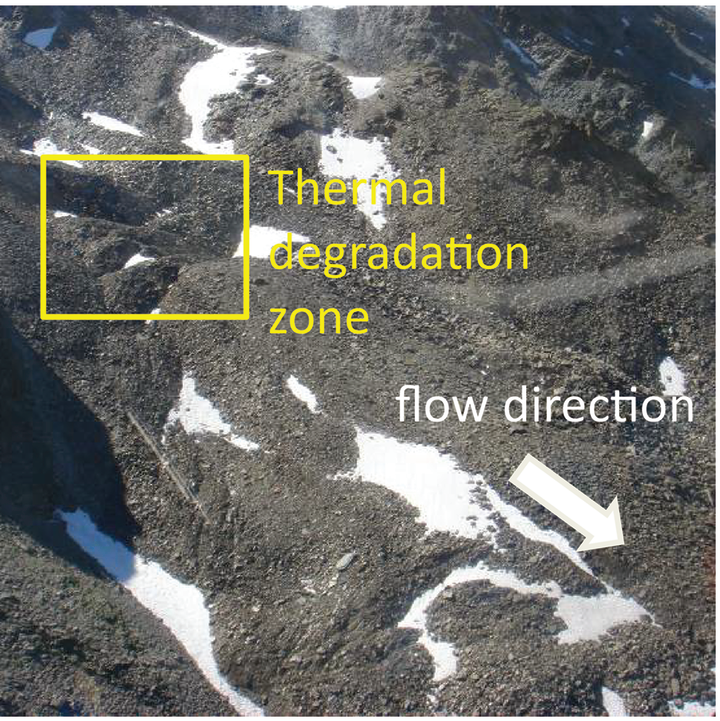
Thermal degradation zone
flow direction

(a)

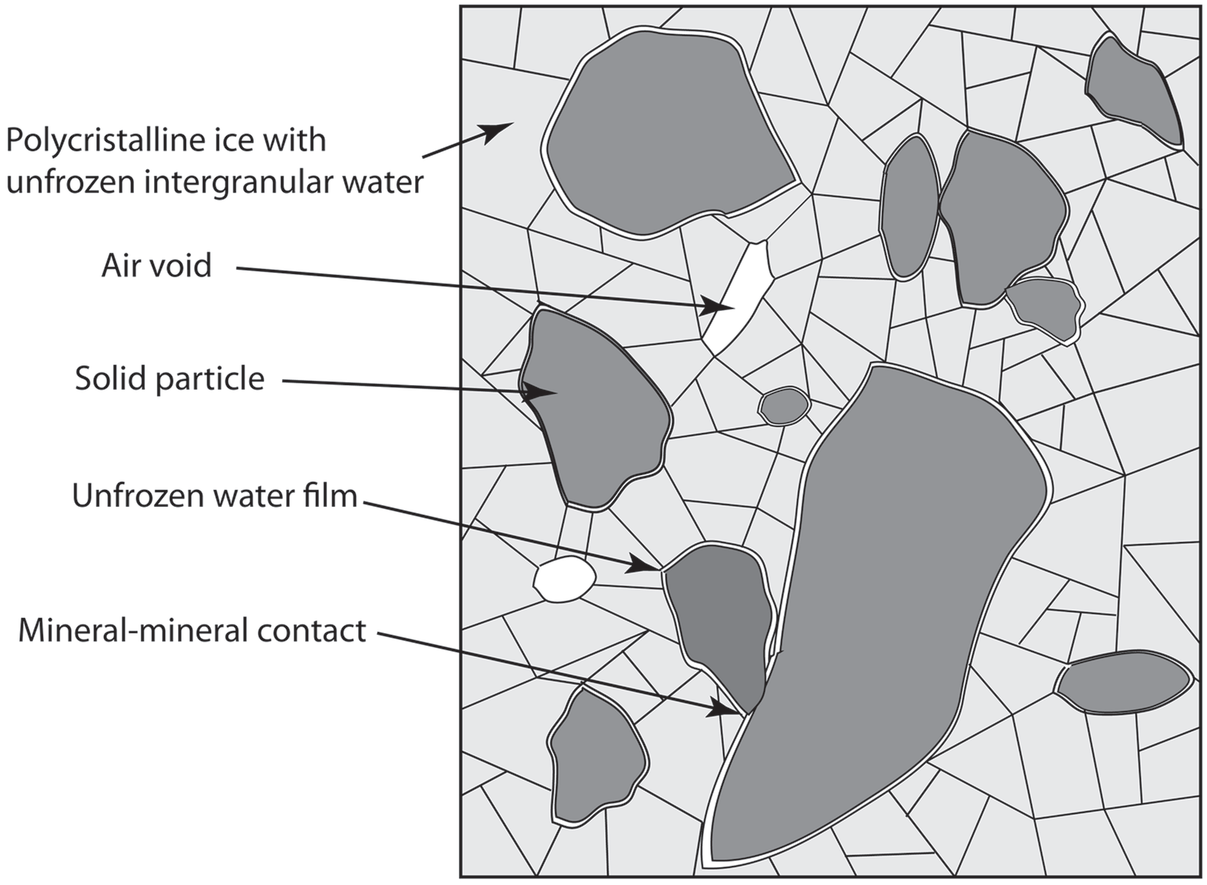
Polycristalline ice with unfrozen intergranular water
Air void
Solid particle
Unfrozen water film
Mineral-mineral contact

(b)

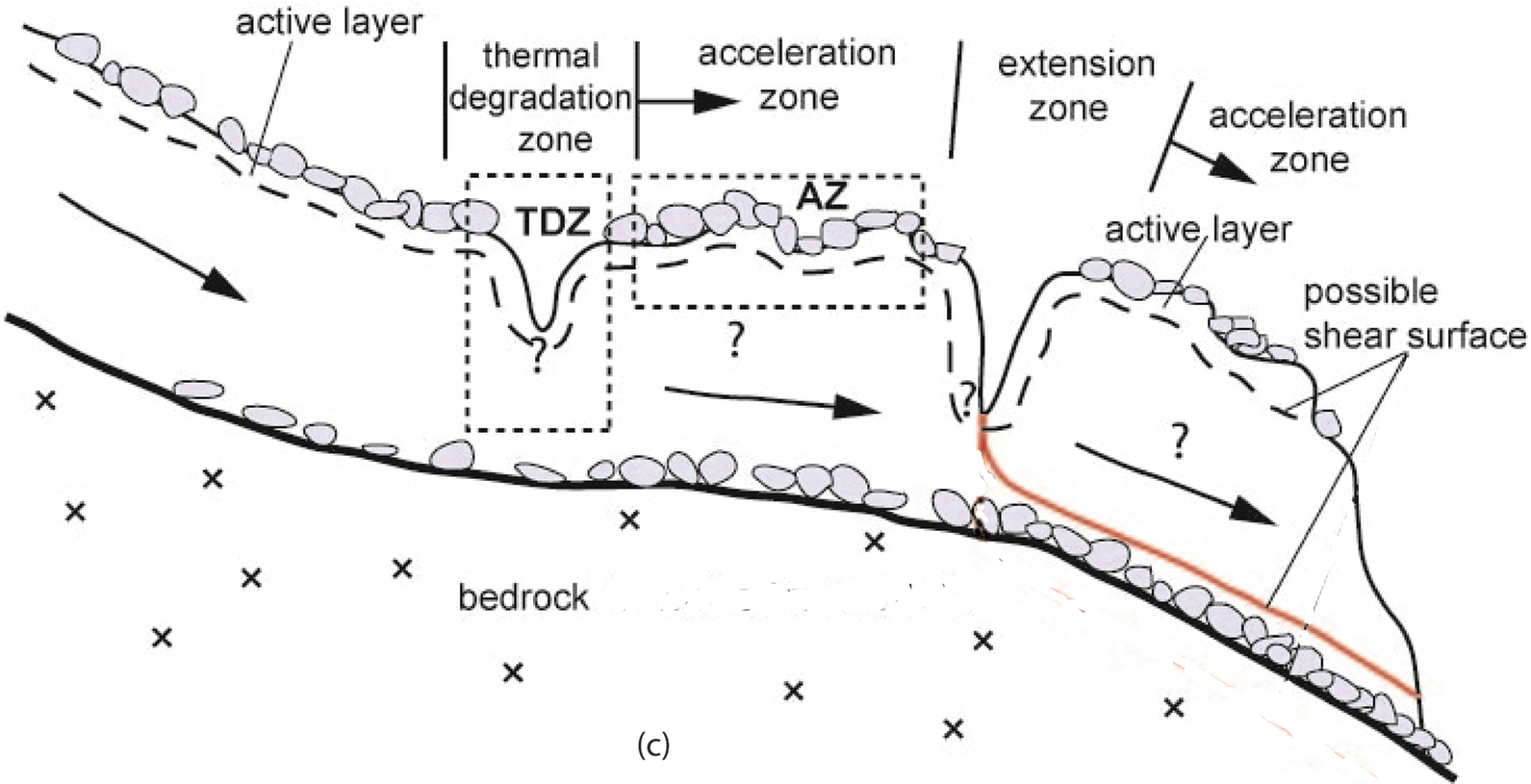
active layer
thermal degradation zone
acceleration zone
extension zone
acceleration zone
TDZ
AZ
active layer
possible shear surface
?
?
?
?
bedrock

(c)

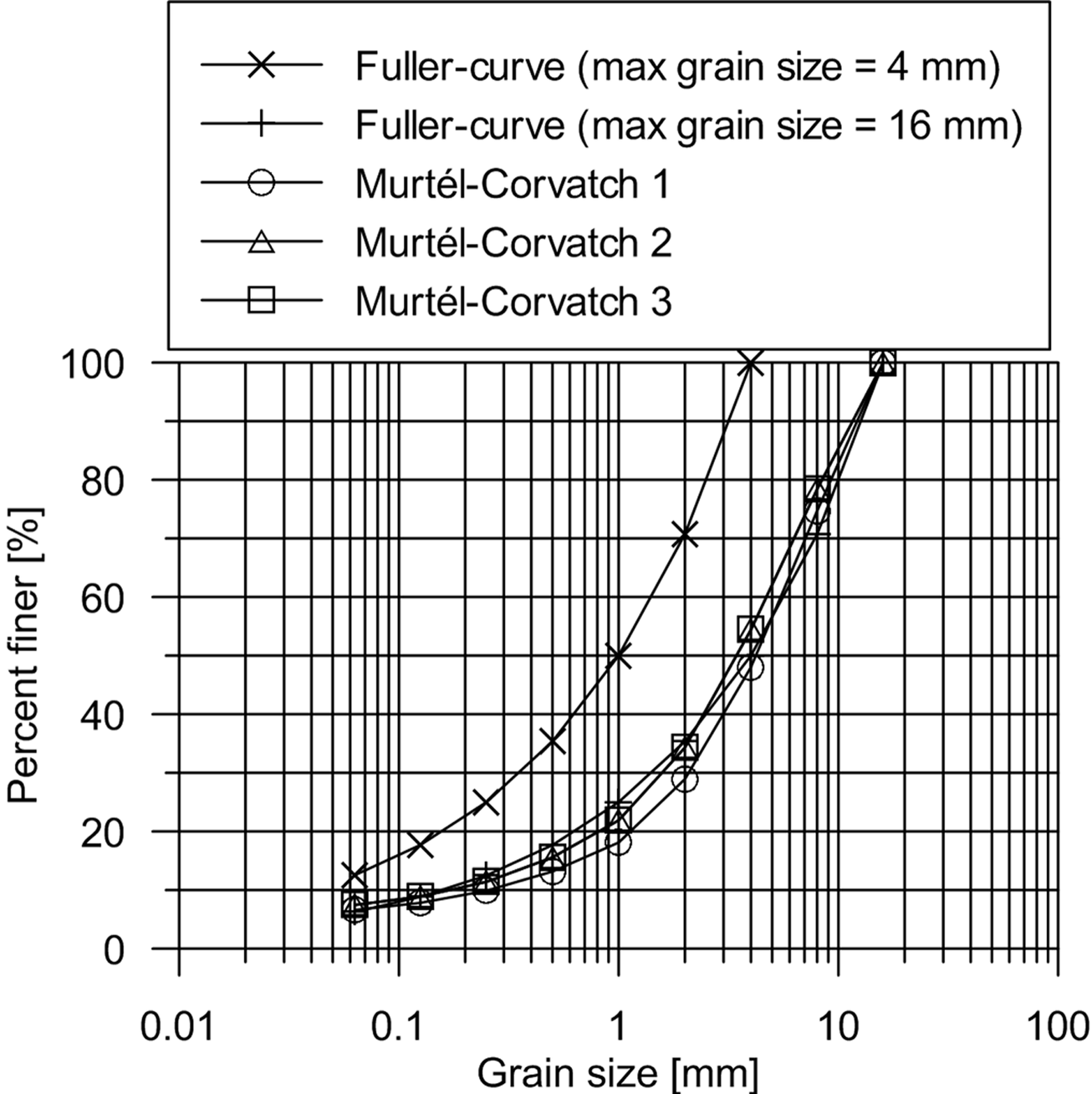
Fuller-curve (max grain size = 4 mm)
Fuller-curve (max grain size = 16 mm)
Murtél-Corvatch 1
Murtél-Corvatch 2
Murtél-Corvatch 3
100
80
60
40
20
0
Percent finer [%]
0.01
0.1
1
10
100
Grain size [mm]

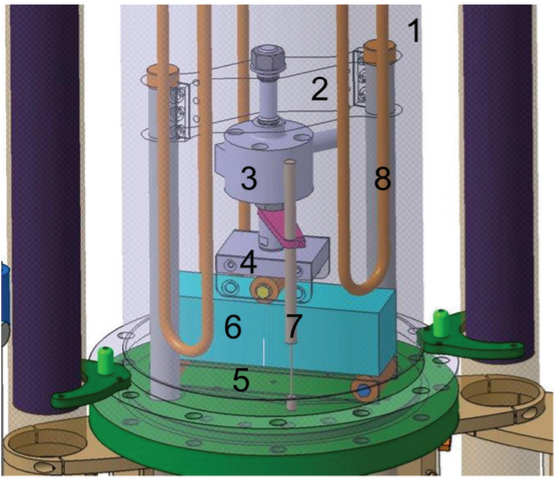

1 – triaxial cell
2 – load frame
3 – load cell
4 – top one point
5 – bottom two points
6 – notched specimen
7 – LVDT
8 – copper tubes

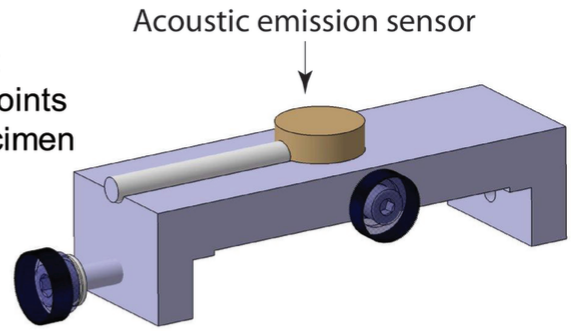

(a)

(b)

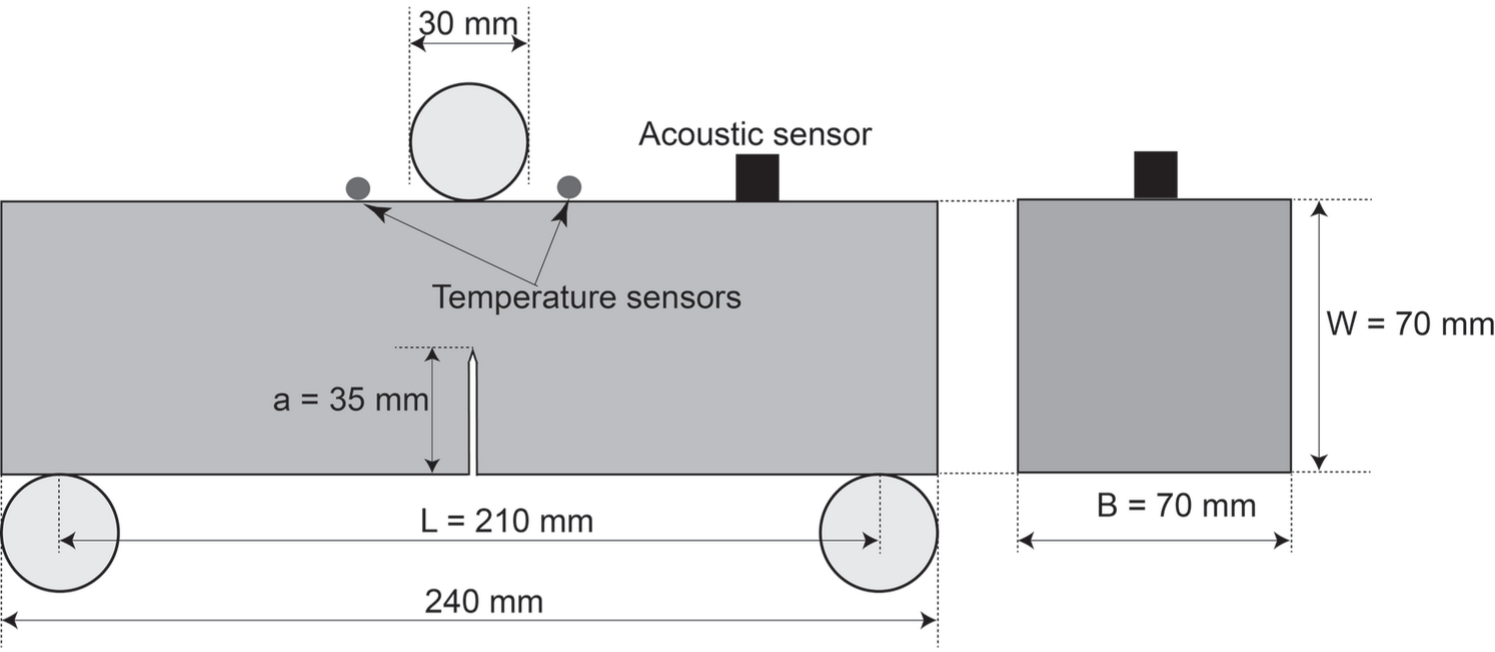

(c)

(d)

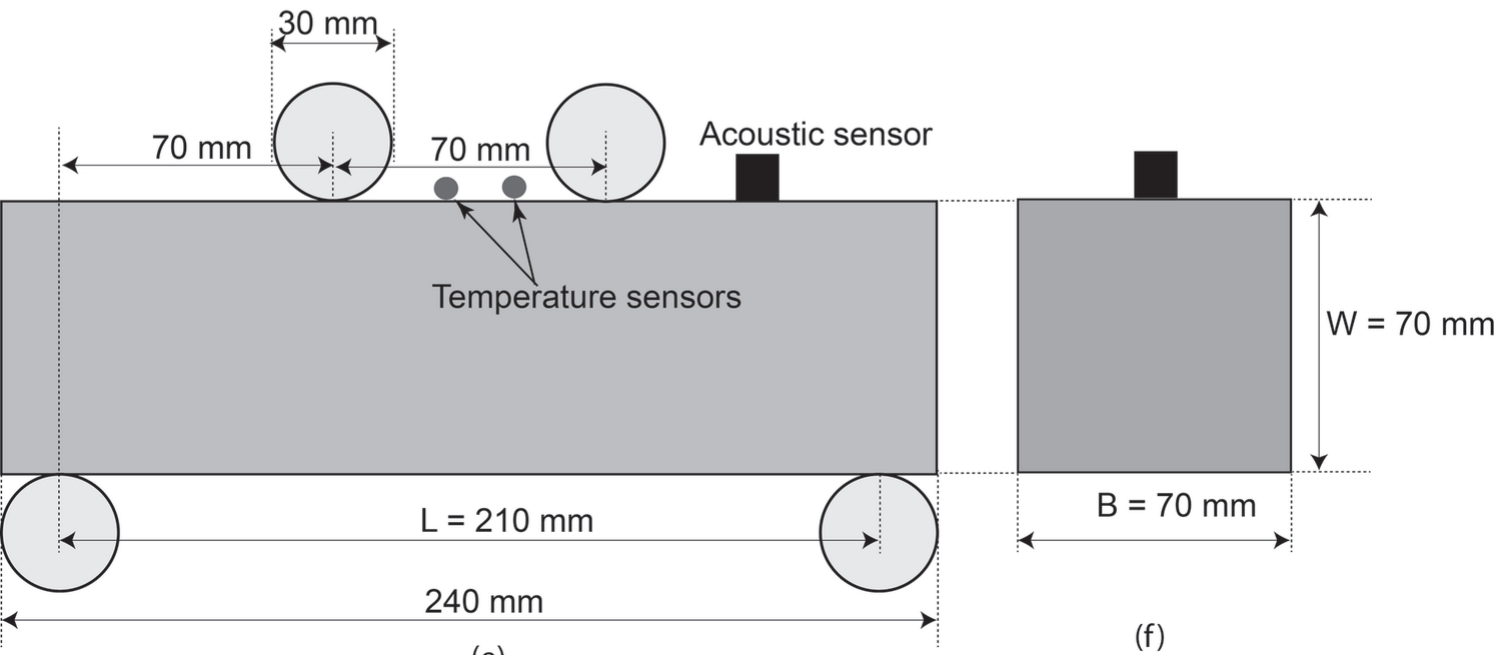

(e)

(f)

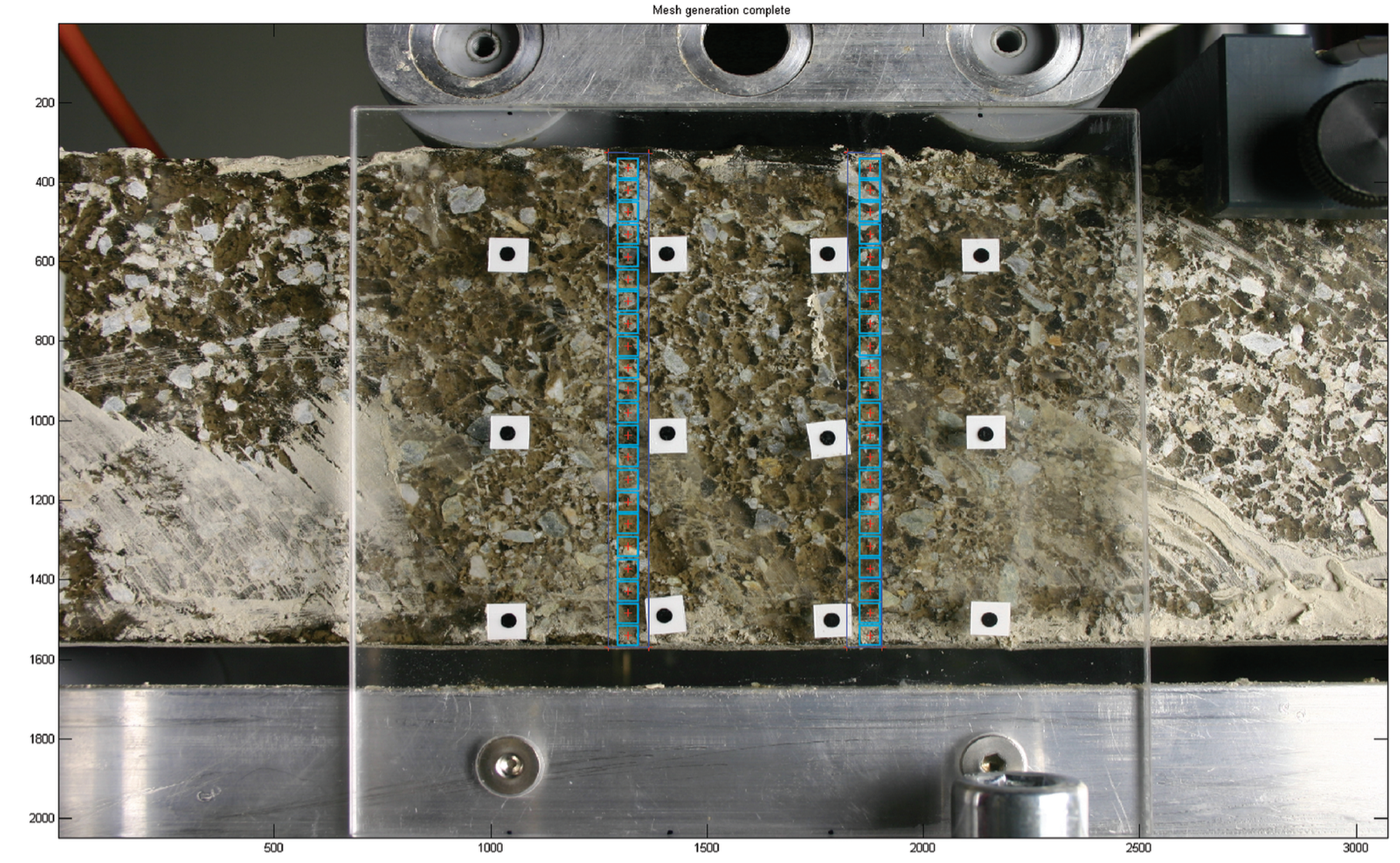
Mesh generation complete
200
400
600
800
1000
1200
1400
1600
1800
2000
500
1000
1500
2000
2500
3000

(a)

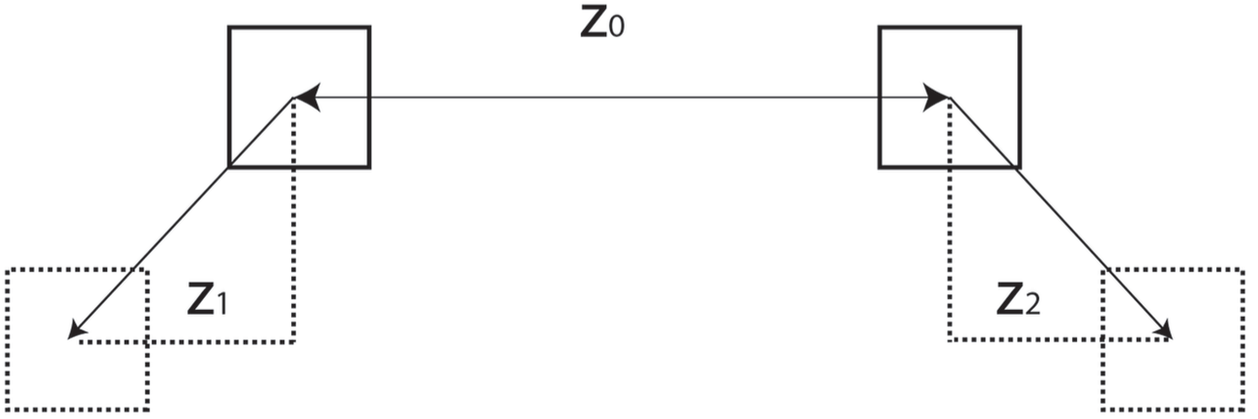
Z0
Z1
Z2

(b)

(a) Displacement rate = 1.0 mm/min

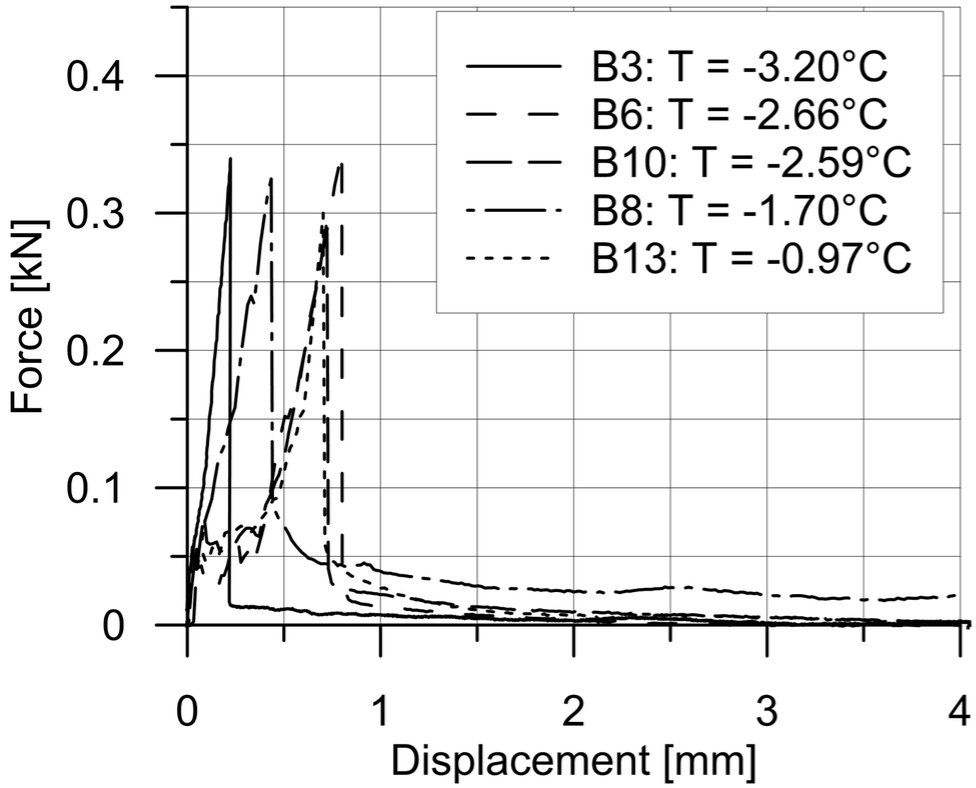

(b) Displacement rate = 0.1 mm/min

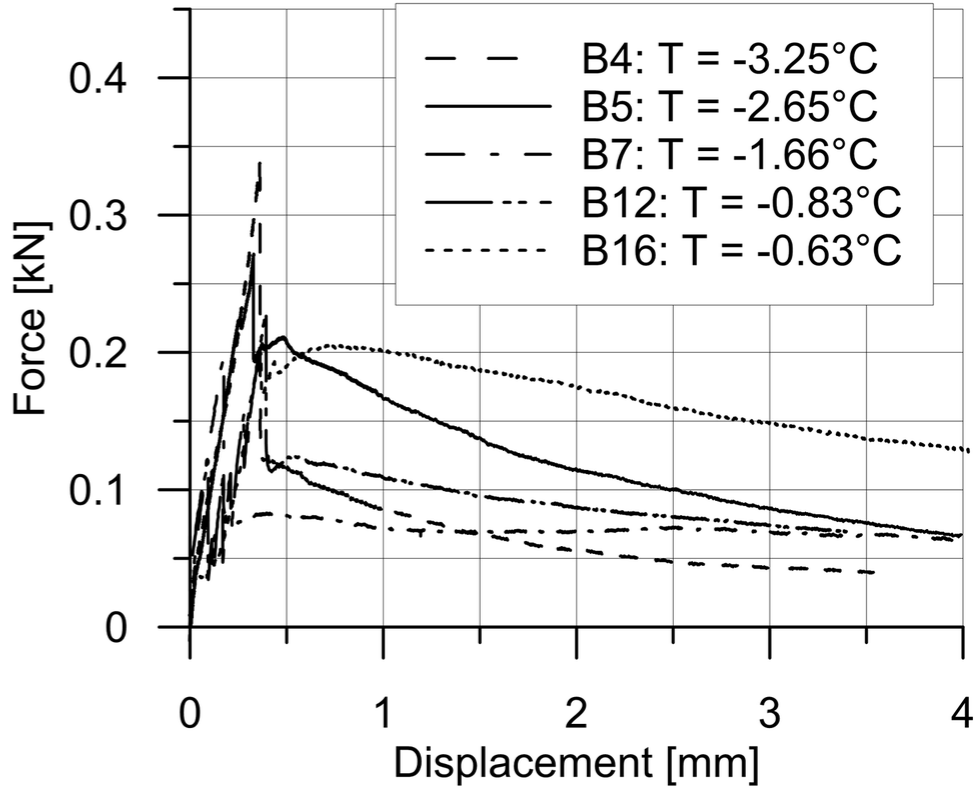

(c) Displacement rate = 0.1 mm/min

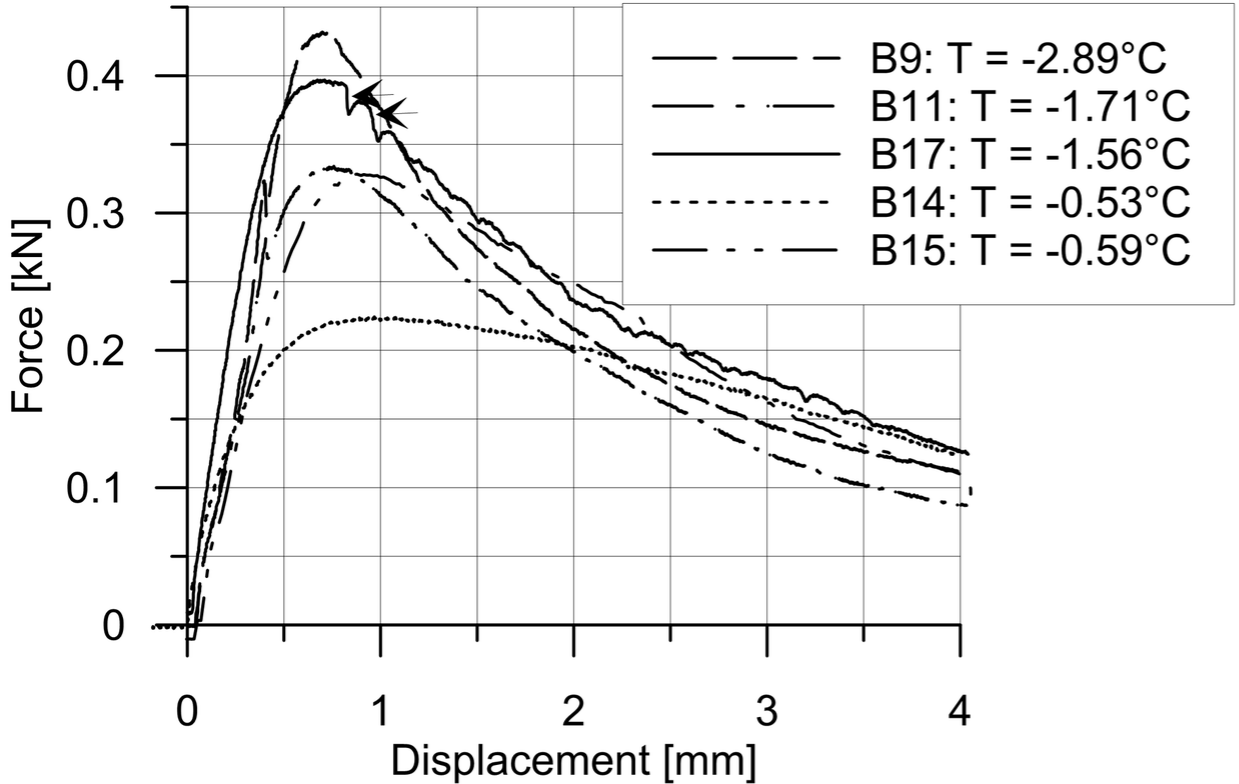

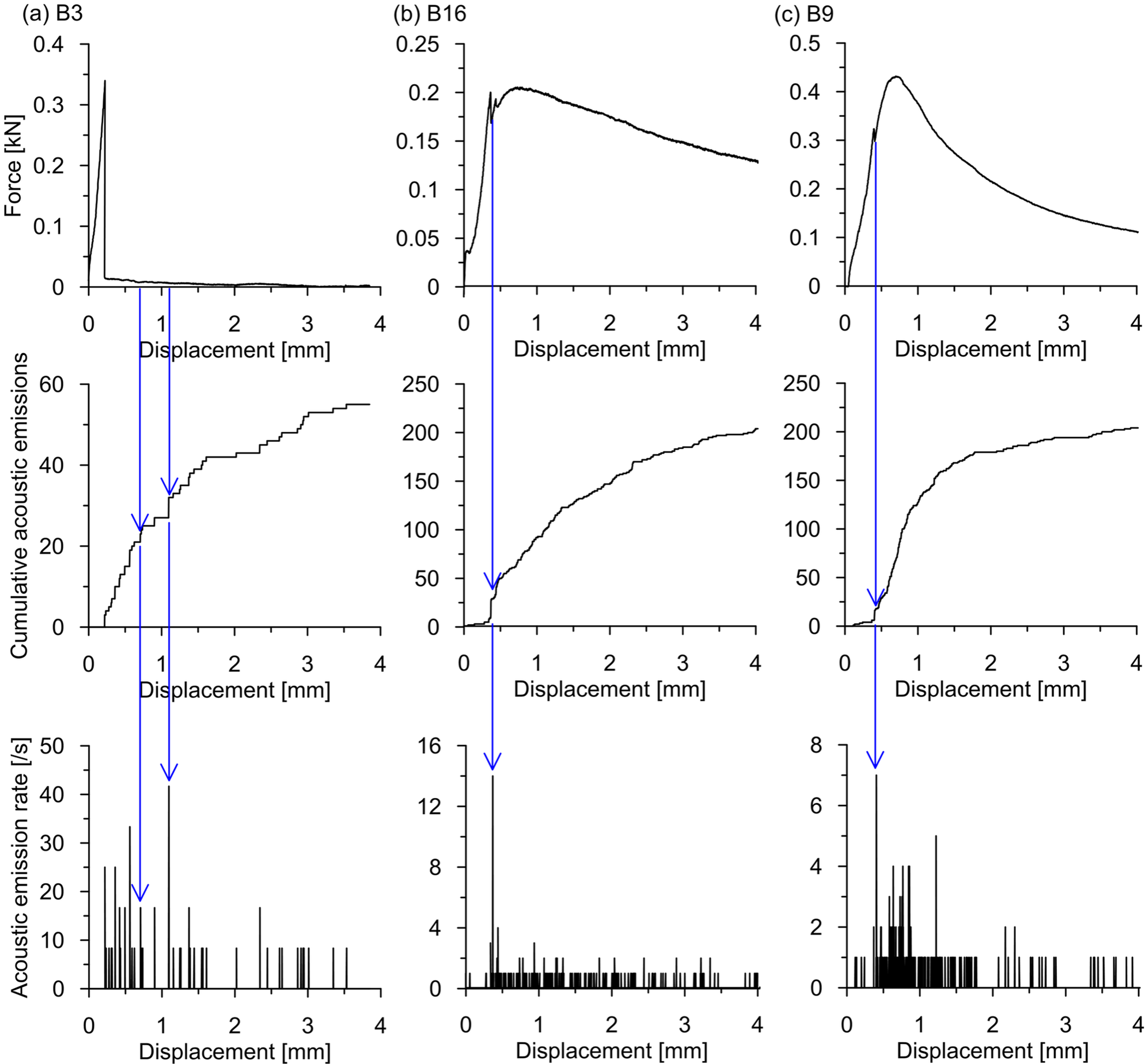
(a) B3
(b) B16
(c) B9
Force [kN]
Cumulative acoustic emissions
Acoustic emission rate [/s]
Displacement [mm]
0.4
0.3
0.2
0.1
0
0.25
0.2
0.15
0.1
0.05
0.5
0.4
0.3
0.2
0.1
60
40
20
0
250
200
150
100
50
50
40
30
20
10
16
12
8
4
6
4
2
0
1
2
3
4

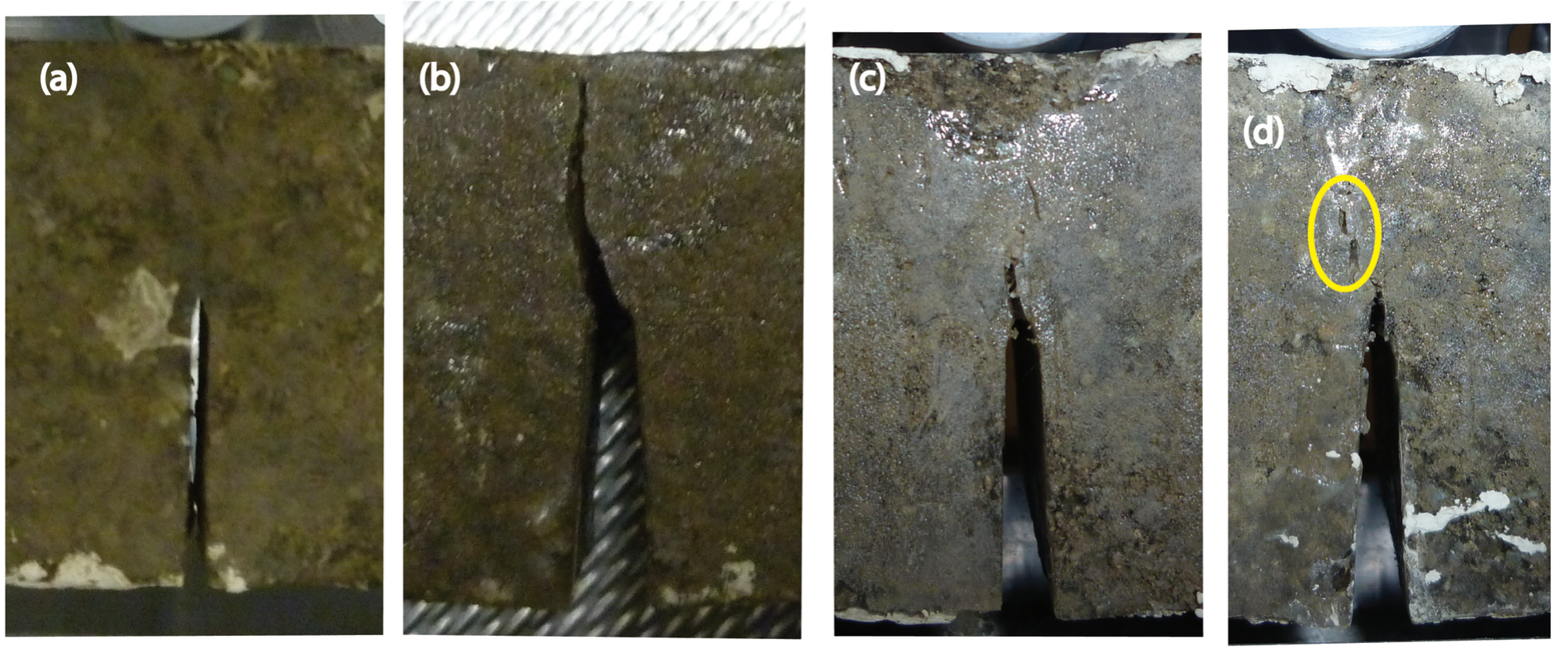
(a)
(b)
(c)
(d)

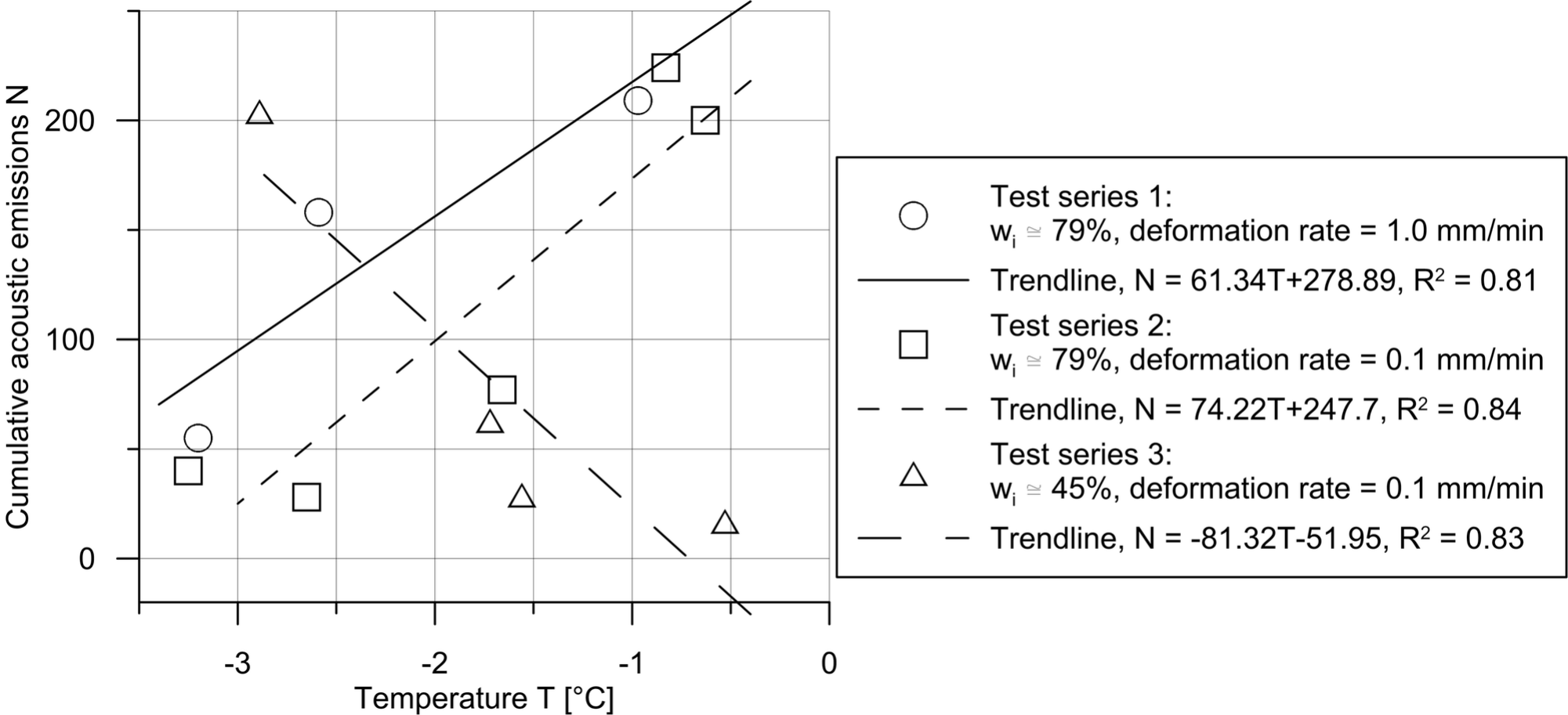
Cumulative acoustic emissions N
200
100
0
-3
-2
-1
0
Temperature T [°C]
Test series 1:
$w_i \approx 79\%$, deformation rate = 1.0 mm/min
Trendline, N = 61.34T+278.89, R^2 = 0.81
Test series 2:
$w_i \approx 79\%$, deformation rate = 0.1 mm/min
Trendline, N = 74.22T+247.7, R^2 = 0.84
Test series 3:
$w_i \approx 45\%$, deformation rate = 0.1 mm/min
Trendline, N = -81.32T-51.95, R^2 = 0.83

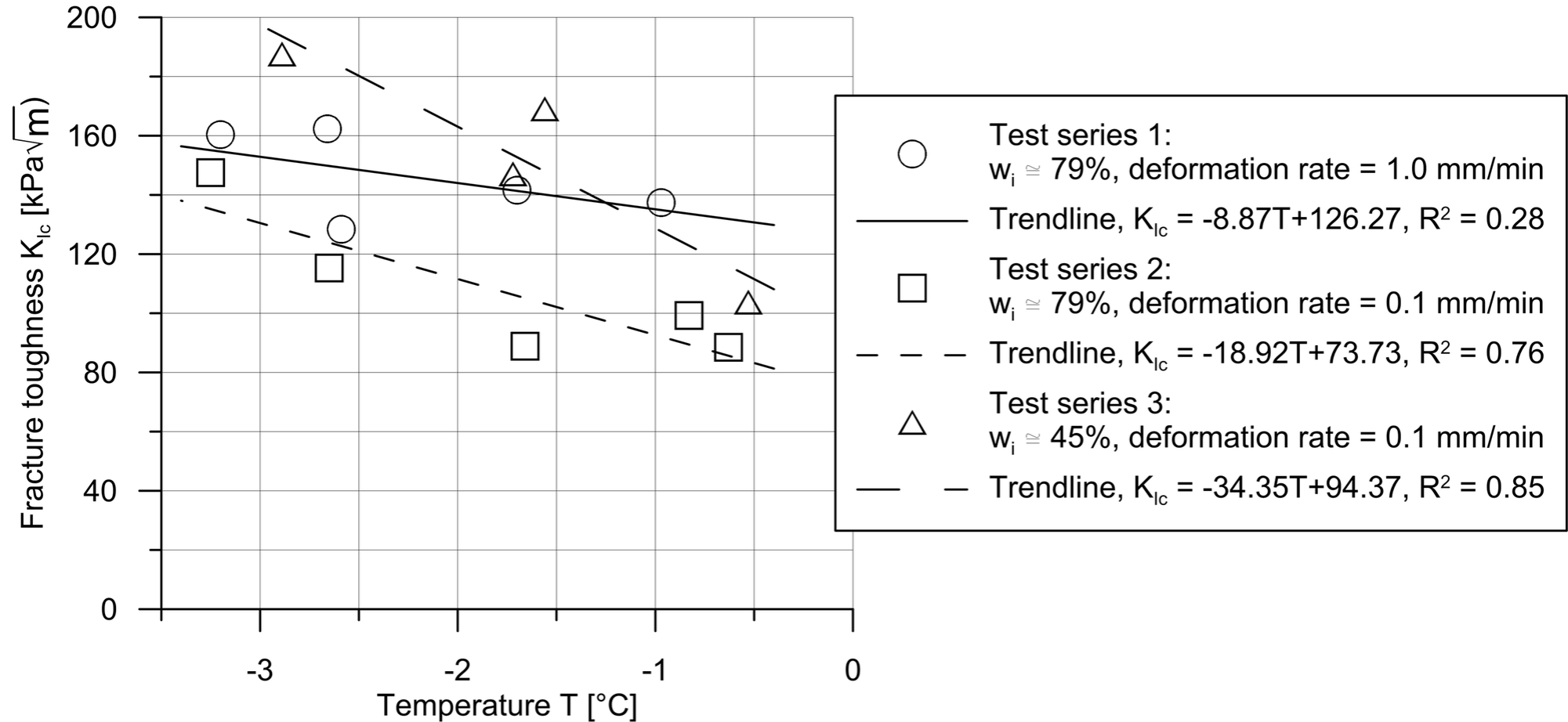
200
160
120
80
40
0
Fracture toughness K_{Ic} [kPa$\sqrt{m}$]
-3
-2
-1
0
Temperature T [°C]
Test series 1:
$w_i \approx$ 79%, deformation rate = 1.0 mm/min
Trendline, K_{Ic} = -8.87T+126.27, R^2 = 0.28
Test series 2:
$w_i \approx$ 79%, deformation rate = 0.1 mm/min
Trendline, K_{Ic} = -18.92T+73.73, R^2 = 0.76
Test series 3:
$w_i \approx$ 45%, deformation rate = 0.1 mm/min
Trendline, K_{Ic} = -34.35T+94.37, R^2 = 0.85

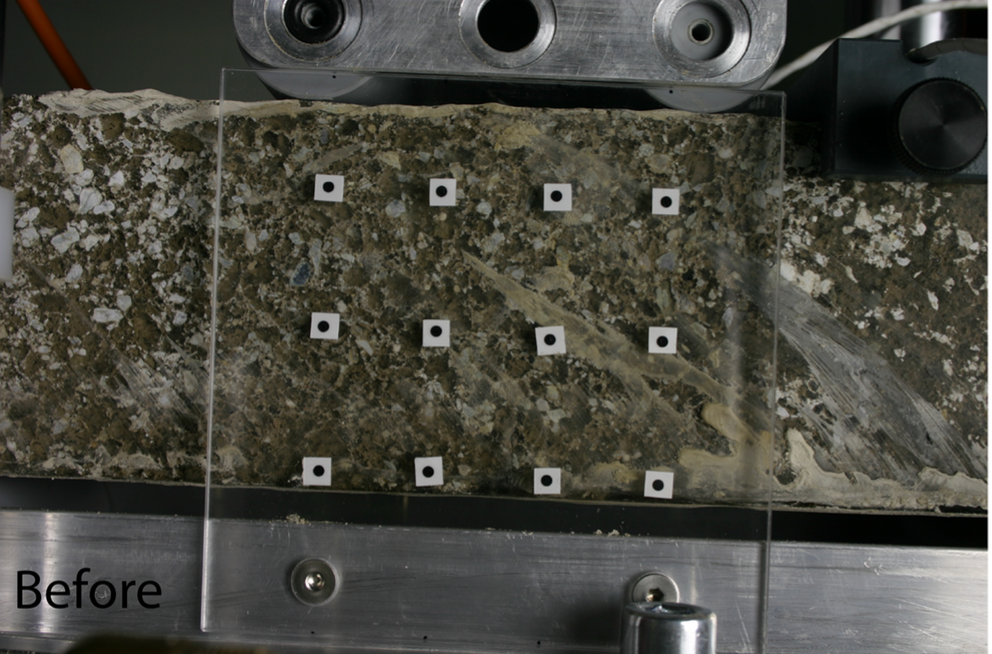

(a)

(b)

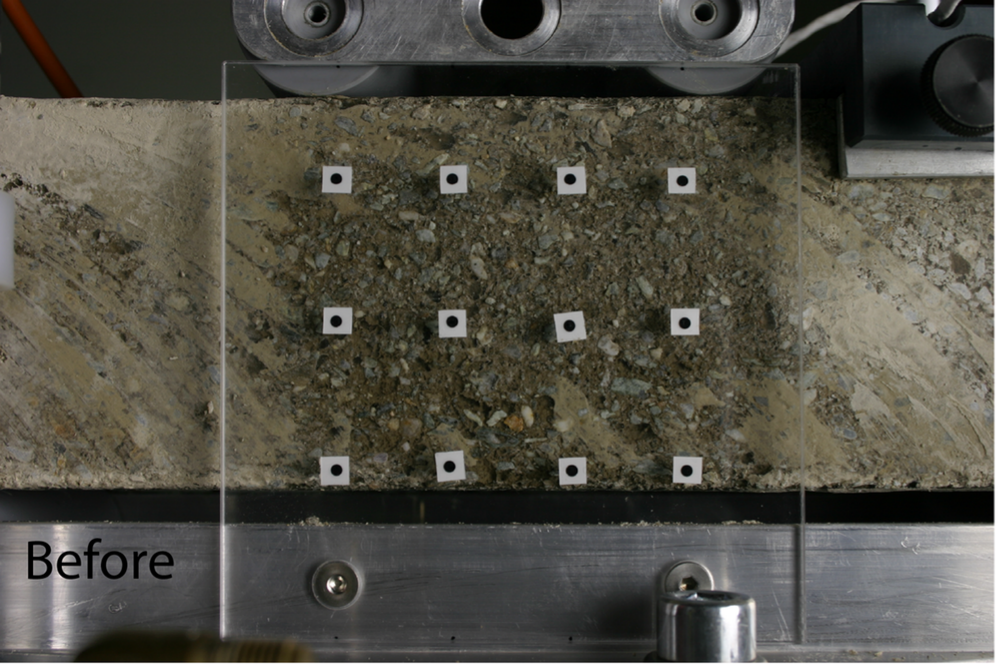

(a)

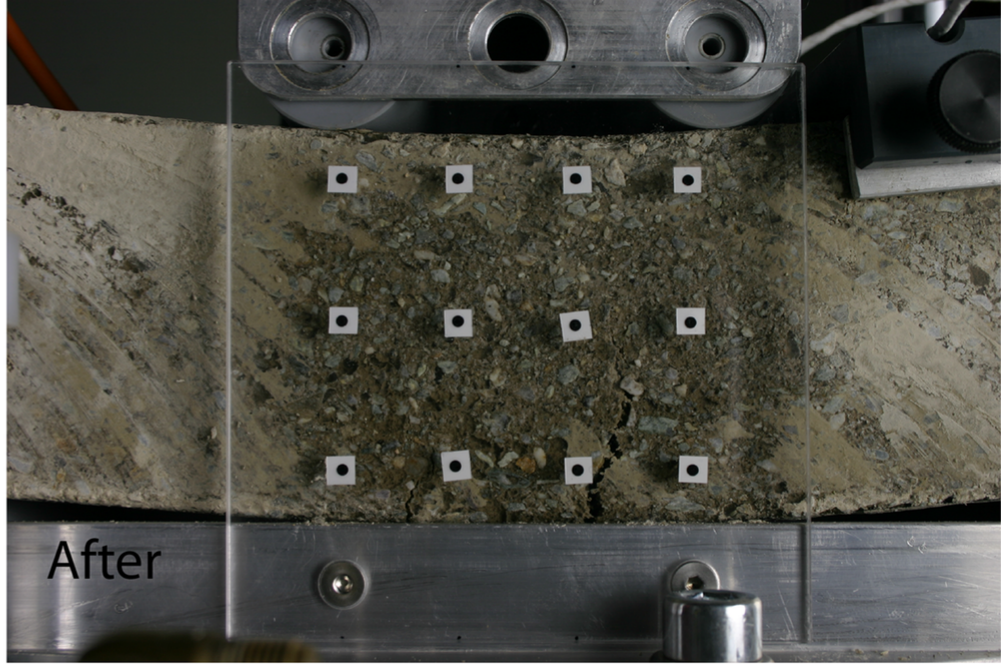

(b)

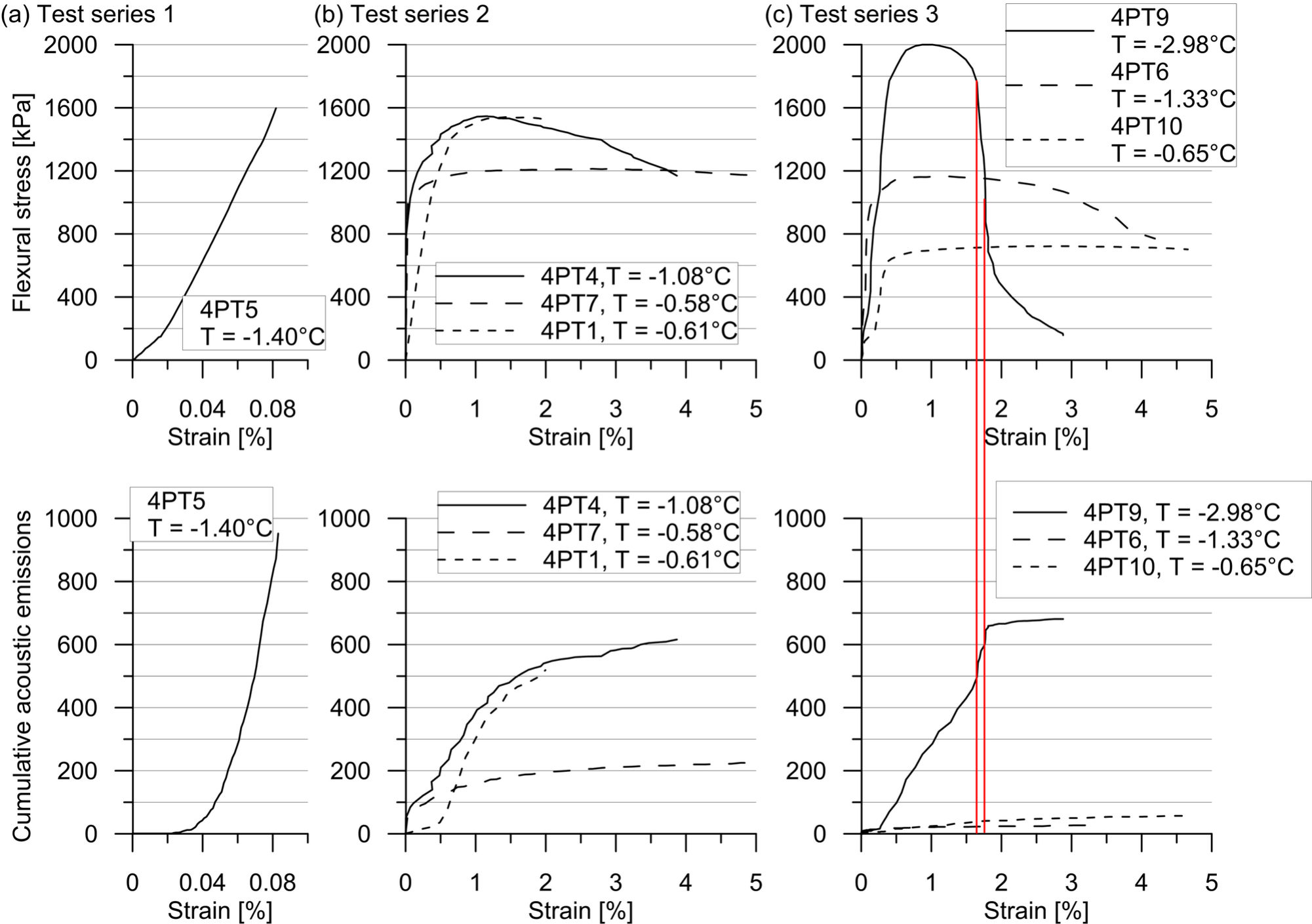
(a) Test series 1
(b) Test series 2
(c) Test series 3
Flexural stress [kPa]
Cumulative acoustic emissions
Strain [%]
4PT5
T = -1.40°C
4PT4,T = -1.08°C
4PT7, T = -0.58°C
4PT1, T = -0.61°C
4PT9
T = -2.98°C
4PT6
T = -1.33°C
4PT10
T = -0.65°C
4PT4, T = -1.08°C
4PT7, T = -0.58°C
4PT1, T = -0.61°C
4PT9, T = -2.98°C
4PT6, T = -1.33°C
4PT10, T = -0.65°C

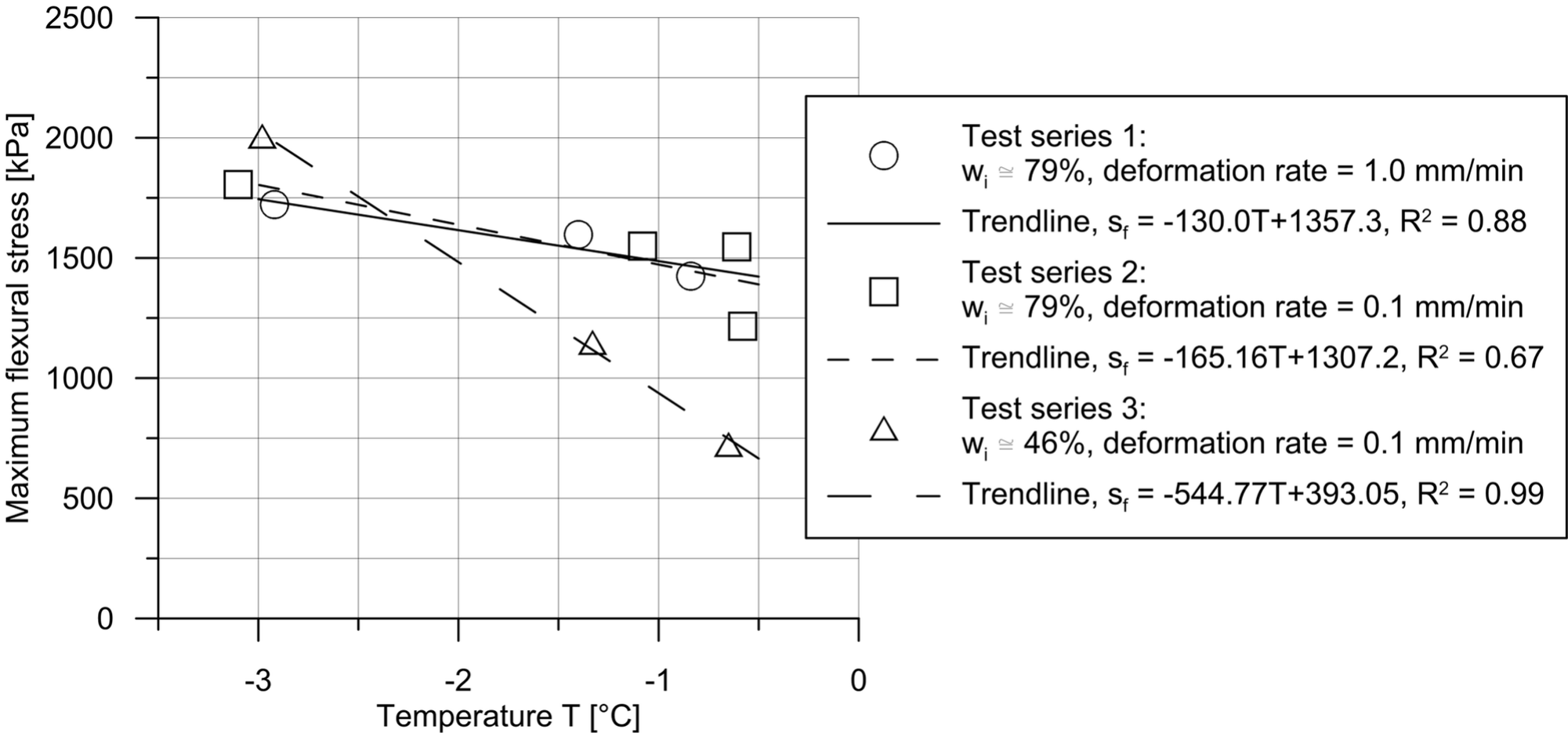
Maximum flexural stress [kPa]
2500
2000
1500
1000
500
0
-3
-2
-1
0
Temperature T [°C]
Test series 1:
$w_i \cong 79\%$, deformation rate = 1.0 mm/min
Trendline, $s_f = -130.0T+1357.3$, $R^2 = 0.88$
Test series 2:
$w_i \cong 79\%$, deformation rate = 0.1 mm/min
Trendline, $s_f = -165.16T+1307.2$, $R^2 = 0.67$
Test series 3:
$w_i \cong 46\%$, deformation rate = 0.1 mm/min
Trendline, $s_f = -544.77T+393.05$, $R^2 = 0.99$